

Shear-flow excitation mechanisms of recessed localized arc-filament plasma actuators

R. R. Kleinman,¹ D. J. Bodony,² and J. B. Freund^{1,2}

¹*Mechanical Science and Engineering, University of Illinois at Urbana-Champaign, 1206 West Green Street, MC-244, Urbana, Illinois 61801, USA*

²*Aerospace Engineering, University of Illinois at Urbana-Champaign, 1206 West Green Street, MC-244, Urbana, Illinois 61801, USA*

(Received 29 April 2010; accepted 23 September 2010; published online 16 November 2010)

Localized arc-filament plasma actuators, placed near the nozzle lip of a laboratory jet, have recently been demonstrated to have sufficient control authority to significantly excite the jet downstream [M. Samimy *et al.*, *J. Fluid Mech.* **578**, 305 (2007)]. This class of plasma actuator, which in this application is recessed in a small cavity near the nozzle lip, causes intense local heating. This heating is thought to be the root mechanism of its influence on the flow, but how this principally entropic thermal source couples with the vortical jet shear layer turbulence downstream is unclear. We investigate this using direct numerical simulations, which match the flow conditions of the corresponding experiment, including Reynolds number, but are two-dimensional to ease computational expense. Despite this obvious modeling approximation, the simulations include the key features of the laboratory system: a thin boundary layer, a plasma-like thermal source in a small recessed cavity, a nozzle lip, and a downstream free shear layer. Results are shown to match the temperature and near-field pressure measured in the laboratory actuators. It is found that the cavity, which was initially included to shield the actuator plasma from the flow, is essential for its action. Thermal expansion within the cavity leads to an ejection of fluid from it, which perturbs the boundary layer and the downstream mixing layer. There is a finite baroclinic torque, but its effects are relatively minor. An alternate actuator designed to mimic the pressure effects of the full actuator, without its concomitant thermal heating, is nearly as effective at exciting the shear layer. An actuator model without the cavity recess does not provide effective actuation. These results suggest that there is significant potential to optimize the actuation authority through design of cavity recesses that augment its effect. © 2010 American Institute of Physics. [doi:10.1063/1.3507317]

I. INTRODUCTION

Passive controls have shown some success reducing the radiated noise from jets.^{1–6} However, these methods often introduce unacceptable drag or thrust penalties. Active control technologies by their time-dependent nature offer the promise of increased control authority with a reduction of loss since they can be turned off.^{7,8} A recent work on the development and characterization of plasma actuators has shown that they have significant control authority and provide an advantage over fluidic-based actuators by being mechanically simpler and relatively lightweight.⁹

Plasma actuation of different types is being considered for a range of flow control objectives. Dielectric barrier discharge (DBD),¹⁰ DC and RF glow discharge,^{11,12} and arc-filament discharge^{8,9,13,14} plasmas, among others, are all being actively researched for applications in boundary layer separation control, shock-wave control, noise mitigation, and shear-flow mixing enhancement. The primary mechanisms by which these types of plasmas interact with the flow make each type best suited for different control objectives in different flow regimes. For example, DBD actuators produce electrohydrodynamic interactions by accelerating charged molecules via a Coulomb force and in that way can locally accelerate a flow. This technology has been used effectively for boundary layer separation control for airfoils.¹⁵

However, it does not appear that DBD and glow discharge actuators have sufficient authority to affect high-speed (near-sonic or above) flows.¹⁶ Arc-filament discharge actuators seem to be better suited to this case. They are thought to generate pressure perturbations via rapid thermal (Joule) heating by the ionized gas established in their vicinity.¹⁴ This effect has been shown to be strong enough to produce shock waves and flow separation in supersonic boundary layers.¹⁷ Arc-filament actuators have also demonstrated the capability to excite strongly amplified instabilities in high-speed jets,⁹ making them a promising technology in aeroacoustic control and jet noise reduction.

The specific localized arc-filament plasma actuators (LAFPA) under consideration here match those under continued development at The Ohio State University (OSU) by Professor M. Samimy and colleagues with the intent of controlling subsonic and supersonic jets⁹ and cavity flows.¹⁸ Depending on the forcing applied, these actuators have increased downstream mixing⁹ and modestly reduced far-field noise relative to an unforced baseline jet.¹⁹

These successful demonstrations are encouraging, but it is still unclear how the LAFPA might be designed and used most effectively since the detailed mechanism by which they act on a flow remains unclear. Determining this mechanism is our goal. The generated plasma is known to quickly create

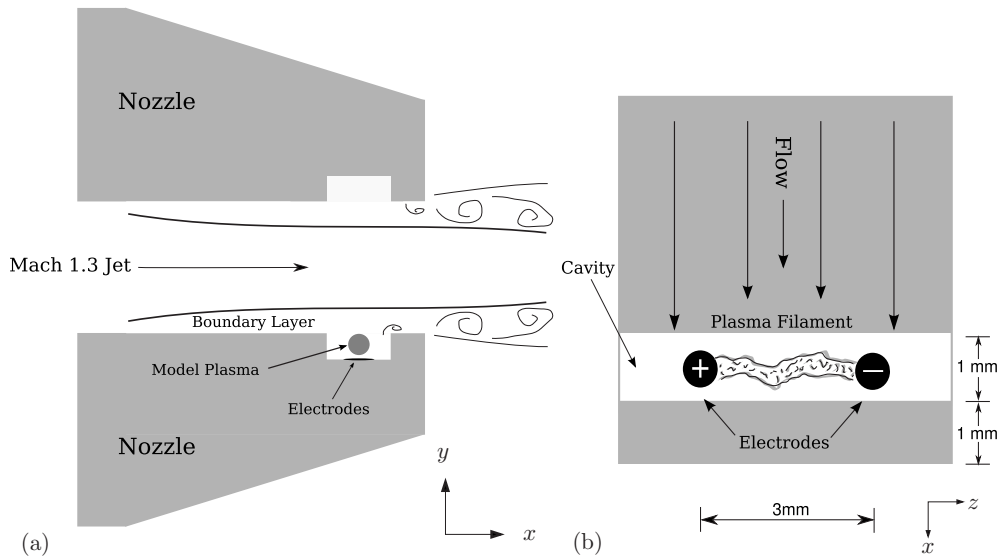


FIG. 1. The OSU Mach 1.3 jet nozzle and the plasma actuator cavity. (a) Side view showing the cavity and (b) top view showing the actuator electrodes and arc-filament plasma within the cavity. The cavity is 0.5 mm deep. Note: this schematic is not drawn to scale.

a local high-temperature region, which is thought to be the root forcing mechanism.^{9,14} What is not known is how this thermal source (an “entropy mode” in a linear sense) alters the flow and drives the observed downstream response (“vorticity mode”) in the jet’s initial shear layers.

In the OSU jet experiments, the arrays of electrode pairs that create the plasma are recessed in a rectangular cross-section cavity near the nozzle outlet as shown in Fig. 1. This cavity forms a ring-shaped groove around the inner circumference of the nozzle. It was added to stabilize the plasma by shielding it from the flow.¹³ However, our results suggest that this cavity recess is fundamental to the mechanisms of flow actuation.

Experimental diagnostics of the actuation are difficult because the plasma emits strong electromagnetic radiation and because of the relatively small dimensions and the harsh high-speed and high-temperature environment. Thus, we have designed a high-fidelity compressible-fluid simulation model to supplement and extend the observations of the experiments to identify the basic forcing mechanisms leading to excitation of the flow downstream. The model includes both the cavity recess and the near-nozzle shear layer of the jet and it closely matches both the cross-sectional actuator geometry and the Reynolds number based on the boundary layer momentum thickness of the OSU experiments. Though it is a two-dimensional model, it does include what are expected to be the key elements of the actuation: the injection of thermal energy due to the plasma, the cavity recess, the nozzle edge, and the early development of the shear layer. Validation against multiple experimental observations supports this. A more realistic fully three-dimensional simulation at the jet Reynolds number would be much more computationally expensive at a comparable flow fidelity. Three-dimensional effects that will be missed with this model are any lateral fluid motion caused by the finite span of actuators and any transition to turbulence. Recently, Gaitonde²⁰ used a highly simplified thermal-patch actuator model in three-

dimensional simulations of forced jets. These allowed for a detailed study of the downstream evolution of the jet and more direct comparisons with experimental measurements of the same. Our focus is on the actuator neighborhood.

Details of the experimental parameters of the jet and the LAFPA system at OSU are given in Sec. II. A full description of the numerical model of the LAFPA is described in Sec. III. Simulation details and numerical methods used specifically for the simulation of the flow in this study are presented in Secs. IV A and IV B, respectively. The results of the simulations are presented and discussed in Secs. V–VII, with conclusions reiterated in Sec. VIII.

II. CHARACTERISTICS OF THE LAFPA

The LAFPA system is implemented on a high-speed, high-Reynolds-number jet used in ongoing experiments at OSU. Relevant details of the flow facility and experimental conditions are described briefly here, but a full description is provided by Samimy *et al.*⁹ The standard experiments consist of a Mach 1.3 axisymmetric jet with a Reynolds number of $Re_D = 1.1 \times 10^6$ based on the jet exit diameter $D_j = 2.54$ cm and the jet centerline velocity. The jet is operated as near to an ideally expanded condition as possible.

A boron nitride nozzle extension attached to the nozzle houses the plasma actuators as shown schematically in Fig. 1(a). A rectangular cross-section groove of width $L_c = 1$ mm and depth $D_c = 0.5$ mm (an aspect ratio of $L_c/D_c = 2$) is machined into the nozzle extension 1 mm upstream of the exit. The plasma is generated between two electrodes spaced 3 mm apart (in the azimuthal direction) in the bottom of the groove as seen in Fig. 1(b). Our two-dimensional model can be considered a cross section down the middle of this approximately two-dimensional system. Visual observation during experiments confirms that the plasma glow is always located inside the cavity. The time dependence of a pulse is approximately a square wave, with

the on-time fraction called the duty cycle. The maximum power is approximately 100 W while the actuator is on.

III. NUMERICAL PLASMA THERMAL MODEL

Numerical models of several different plasmas have been formulated using a combined Navier–Stokes/Maxwell equations approach.²¹ In many cases, these models are necessarily complex due to the complexity of the underlying plasma physics. However, the principal effect of the present arc discharge on the surrounding flow is thought to be a rapid and intense localized heating, which we can model as a time-varying, spatially distributed source of internal energy. Such an approach was followed in the one-dimensional model of Utkin *et al.*¹⁴ We have incorporated a similar thermal-source model into the overall direct numerical simulation model.

Based on the available experimental data,^{9,13,14,22} the plasma is assumed to be a cylindrical heat source with length $L_{\text{act}}=3$ mm and a radius of $r_0=0.25$ mm based on the spacing of the electrodes and observations of the plasma. The thermal source added to the right-hand side of the governing energy equation is

$$S_{\text{act}}(r, t) = w(t) \frac{f(r)}{f_V} \frac{P_{\text{act}}}{\pi r_0^2 L_{\text{act}}}, \quad (1)$$

where the spatial distribution is

$$f(r) = \frac{1}{2} \left[\tanh \left\{ -\sigma_{xy} \left[r(x, y) - \frac{2}{3} r_0 \right] \right\} + 1 \right] \quad (2)$$

and the distance is $r = \sqrt{(x - x_{\text{act}})^2 + (y - y_{\text{act}})^2}$, with x and y the streamwise and cross-stream coordinates as shown in Fig. 1. The source is centered at $(x_{\text{act}}, y_{\text{act}})$, the geometric center of the cavity. The constant $\sigma_{xy} = 10/r_0$ was selected so that $f(r)$ becomes effectively zero before reaching the cavity walls. The power imparted to the flow by the plasma ($P_{\text{act}} = 100$ W) is divided by the volume of the 3 mm long cylinder f_V , as it would be in three dimensions.

The time-varying portion of the source term models the square-wave input signal as

$$w(t) = \frac{1}{2} \left[\tanh \left(\frac{t - t_i}{t_r} \right) - \tanh \left(\frac{t - t_f}{t_r} \right) \right], \quad (3)$$

which allows for a variable duty cycle. This form for $w(t)$ was chosen over a simple pulse-train square wave to facilitate discretization with the numerical solver described in Sec. IV B. The constants are as follows. The time $t_r = 1$ μs is the rise time of the actuator signal (the time for the input signal to go from zero to one), which is less than the time for a compression wave at ambient sound speed to propagate across the cavity recess. The plasma itself is expected to break down much faster than this, but there are no complete measurements of the rate of energy deposition into the fluid once this occurs. The parameter $t_i = 10$ $\mu\text{s} * f_{\text{act}}$ is the time delay of the actuator signal from its driving controller and $t_f = t_i + p_{\text{dc}} T_{\text{act}}$ governs the actuator “off” time and is based on the duty cycle p_{dc} . Of the timing parameters in the simulations using this model, only the duty cycle is varied, not f_{act} , the frequency of actuation.

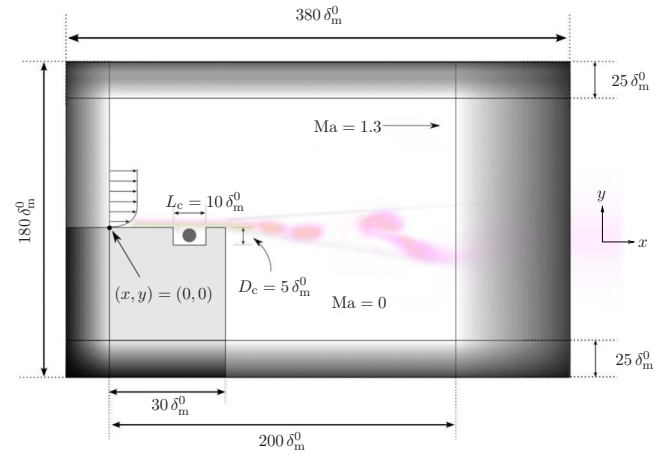


FIG. 2. (Color online) Schematic of the computational domain (not to scale). Dimensions are presented in terms of the momentum thickness at the nozzle exit $\delta_m^0 = 0.1$ mm. The light gray area denotes computational space treated as a solid, isothermal wall. The shaded area on all four sides of the domain denotes the absorbing buffer zones. The dark circle located in the cavity shows the location of the internal energy source in Eq. (1).

IV. SIMULATION DETAILS

A. Flow domain and parameters

The numerical plasma model of Sec. III is incorporated as an internal energy source in the compressible flow equations in two dimensions. No modeling is used in the fluid flow solution. The equations are nondimensionalized by the speed of sound $c_\infty = 343$ m/s, density $\rho_\infty = 1.2$ kg/m³, viscosity $\mu_\infty = 1.87 \times 10^{-5}$ kg/(m s), temperature $T_\infty = 300$ K, and the experimentally estimated momentum thickness at the exit of the jet $\delta_m^0 = 0.1$ mm. Based on these values, the momentum thickness Reynolds number is $\text{Re} = 3330$. The Prandtl number is $\text{Pr} = 0.7$. Despite the locally high temperatures we shall see near the actuator, the ideal gas model is chosen to close the system of equations.

The simulation domain covering the near-nozzle region of the OSU experimental jet is shown schematically in Fig. 2. The basic flow is a Mach 1.3 compressible boundary layer above a solid wall at $y=0$ with fixed wall temperature equal to T_∞ . There is no flow ($\text{Ma}=0$) downstream of the nozzle exit for $y \leq 0$. All wall boundaries are isothermal. With the inclusion of the thermal source from Sec. III, some amount of heat transfer from the cavity fluid to the boron nitride nozzle extension is expected, but we do not model this beyond recognizing that an isothermal boundary should provide a good model since the thermal conductivity of the nozzle is high and the actuators are small thermal sources relative to the size of the whole nozzle.

The laminar inflow boundary layer is specified above the wall using the method outlined by Lui.²³ The actual boundary layer leaving the nozzle lip at these conditions is too thin for its profile to be accurately measured. Estimates from experiments using a nozzle with similar length but at different flow conditions suggest that the boundary layer is turbulent with a momentum thickness of around $\delta_m = 0.1$ mm.²⁴ However, using the acceleration parameter $K = \nu / U^2 \partial U / \partial x$ employed by Viswanathan and Clark²⁵ and a Reynolds Aver-

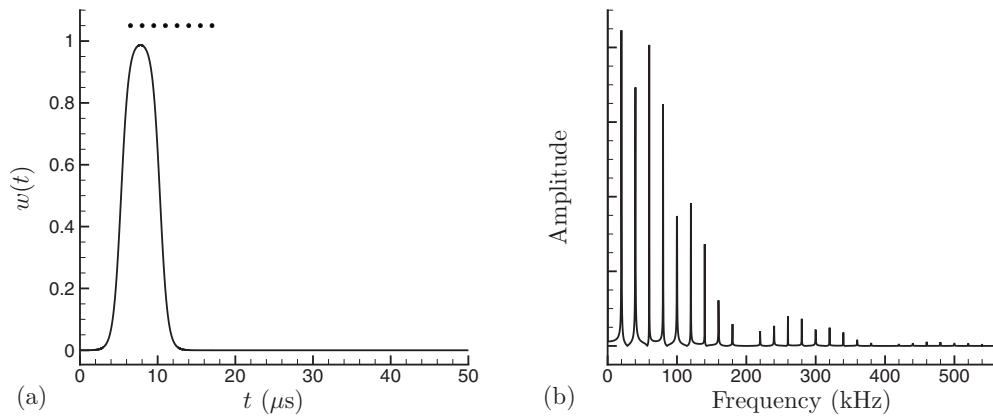


FIG. 3. (a) Time profile of $w(t)$ in Eq. (3) for 20 kHz forcing with 10% duty cycle. The dots correspond to the times visualizations in Sec. VII A. (b) Corresponding frequency spectrum of $w(t)$.

aged Navier-Stokes (RANS) solution of the jet mean flow gradient near the nozzle, the boundary layer in this flow is expected to be laminar. Kearny-Fischer *et al.*²⁶ recently showed that with the nozzle extension that houses the actuators added, the near-nozzle shear layer profile becomes nearly invariant to Reynolds number. However, this is possibly a manifestation of the cavity modes exciting the boundary layer and that the boundary layer encountering the cavity is indeed laminar. We shall see in our two-dimensional simulations at comparable Reynolds number that this does occur. Regardless, a laminar boundary layer is used in the present investigation of mechanisms. The nondimensional momentum thickness of the layer (δ_m / δ_m^0) was specified to be equal to unity at the nozzle exit ($x = 30\delta_m^0$ in Fig. 2). The downstream physical simulation domain extends to $x = 200\delta_m^0$ so that we can study the near-nozzle response of the shear layers. The cross-stream physical domain extends out to $y = \pm 65\delta_m^0$. For reference, in terms of the experimental jet dimensions, the streamwise domain extends to about $x = 0.8D_j$ and the cross-stream domain from $y = \pm 0.25D_j$. A computational absorbing buffer zone of width $25\delta_m^0$ is present above and below the cross-stream physical domain and $30\delta_m^0$ and $150\delta_m^0$ upstream and downstream of the streamwise physical domain, respectively.

B. Numerical methods

A full description of the numerical schemes is reported elsewhere²⁷ and summarized briefly here, in the context of the actuator simulations. The flow equations are solved using high-resolution explicit and compact finite-difference schemes. The resolution optimized finite-difference schemes are used for the interior points of the computational mesh. Fourth-order biased schemes are used at the walls and the edges of the computational domain. The mesh is Cartesian and stretched in both coordinate directions so as to cluster points in the cavity and the shear layer. The functional mappings used to stretch the mesh are also reported elsewhere. The minimum spacings were $\Delta x_{\min} = 0.030\delta_m^0$ and $\Delta y_{\min} = 0.026\delta_m^0$. The mesh had $N_x \times N_y = 3000 \times 1001$ points. A

standard fourth-order Runge–Kutta time algorithm was used for time integrating the flow equations and the numerical time step was $\Delta t c_\infty / \delta_m^0 = 0.005$ (~ 1.45 ns).

The Navier–Stokes characteristic boundary conditions²⁸ with the viscous correction of Yoo and Im²⁹ are used for boundary conditions on the isothermal walls. One-dimensional characteristics are used on the computational domain edges as a radiation boundary condition to disallow nonphysical reflections back into the physical domain. Figure 2 shows shaded areas indicating the boundary buffer zones.^{30,31} Low-order, low-pass filtering is also implemented in these zones to reduce any numerical artifacts generated at these outer boundaries and temper the flow moving toward the boundary. Lastly, numerical stabilization of the flow solutions is provided by high-order, high-wave number filtering in the physical domain of the solution.^{32,33} The flow solution is filtered in both coordinate directions once every five time steps in the physical domain of the simulation. A linear combination of the filtered solution (40%) is combined with the unfiltered solution (60%) at that time step and taken as the new simulation solution. The filtering is purely for numerical stabilization and is confirmed not to alter the physical behavior of the flows simulated here, as well as in other flows.³³ The present results were also confirmed to be mesh and stabilization independent.

C. Actuator forcing parameters

The forcing frequency was $f_{\text{act}} = 20$ kHz for all simulations, which was chosen for its experimental relevance,⁹ and simulated duty cycles of 5%, 10%, and 20% duty cycle also match corresponding experimental data. Using these forcing parameters, the time input signal (3) and the corresponding frequency spectra of the forcing are shown in Fig. 3.

D. Simulation procedure

Each simulation presented here was advanced in time from the parallel-flow initial condition for 1×10^6 time steps to allow for initial flow transients to convect out of the domain. The actuator model is active during this initial simula-

tion. Statistical data are then collected during the following 2×10^6 time steps. This corresponds to 33 domain flow-through times (based on advection velocity $0.65U_\infty$) and 58 actuator forcing periods, respectively. Phase-averaged quantities presented in the following sections are averaged over all of these 58 forcing periods.

V. EXPERIMENTAL COMPARISON

As mentioned in Sec. I, the detailed experimental characterization of the cavity and the near-nozzle region is limited. However, there are two available points of comparison with the experiments that allow us to assess whether the simulations are at least qualitatively in line with the actuators in the experiment. Estimates are available of the temperature of the plasma in the cavity and the sound pressure level (SPL) at a location slightly downstream of the nozzle exit.

A. Near-field pressure

The pressure amplitudes measured for the ideally expanded Mach 1.3 jet are compared with the results of the simulations presented here. The actuation was axisymmetric (i.e., eight actuators firing simultaneously) for a 20 kHz forcing with a 20% duty cycle. The pressure measurement was made at a location where the probe just grazed the edge of the shear layer, half a jet diameter downstream ($x/D_j=0.5$) of the nozzle lip. This corresponds in the simulation to $(x,y)=(127,-20)\delta_m^0$. The experiments report an amplitude of 172 dB at $x/D_j=0.5$, but the trend shows the amplitude decreasing sharply afterward, suggesting a higher reading closer to the nozzle. Our corresponding SPL was 173 dB, which is in close agreement with the experimental data. It should be clear that the pressure at this point is expected to be dominated by fluctuations associated with the flow dynamics and this favorable agreement is not a direct quantitative assessment of the actuator model.

B. Cavity temperature

The second model validation comes from comparing the reported peak plasma temperature and the corresponding maximum temperature of the fluid in the model simulations. The temperature in the experiments is calculated from emission spectroscopy since it was not feasible to measure it with probes. A least-squares fit was then used to compare the measured spectrum and the synthetic spectra from the second positive band system of nitrogen, calculated numerically using temperature as a free parameter. Results of this calculation suggest that the plasma reaches temperatures near 2000 K,³⁴ although depending on the type of power supply, the temperature could be as low as 1200 K.²² The one-dimensional model of Utkin *et al.*¹⁴ suggests a maximum temperature near 1800 K for this particular set of actuation parameters. The phase-averaged temperature in the cavity for 20 kHz forcing at 20% duty cycle is shown to have a maximum temperature of around 1600 K. When the temperature is not phase-averaged, the maximum temperatures of the fluid in the groove do reach slightly over 1800 K at the peak

of the actuator's "on" time. Overall, this appears to be a reasonable agreement, especially given the simplicity of our actuator model.

VI. EFFECT ON NATURAL CAVITY OSCILLATIONS

Cavities, such as that containing the plasma actuator here, are well known to be susceptible to self-sustaining oscillations at discrete frequencies.^{35–38} The observed feedback mechanism between the shear layer instabilities, their interaction with the downstream edge of the cavity, and the receptivity of the acousticlike perturbation at the leading edge are as expected and are quantified in detail for our simulations elsewhere.²⁷ There it is seen that the oscillation frequencies are in the range seen at similar flow conditions in experiments.

Here we are interested in the interaction, if any, of the actuation with these modes, particularly whether this natural resonance is fundamentally altered by the actuation. We expect the plasma to disrupt the resonance when it fires, but we also seek to understand whether it fundamentally upsets this resonance between firings. Most of the time, the actuator is off, even at the highest 20% duty cycles studied. We anticipate that the resonance will be slightly altered even when the actuator is off because the cavity is expected to remain at elevated temperature, which in turn would modestly increase the speed of sound, and thereby should at least marginally increase the frequency of the resonance.

To assess the possible nonstationary features of the cavity spectrum, we introduce a joint time-frequency analysis. The simplest such decomposition is the short-time Fourier transform (STFT), which is defined as

$$\text{STFT}(f,t) = \int_{-\infty}^{\infty} p(\tau)W^*(\tau-t)e^{-2\pi if\tau}d\tau, \quad (4)$$

where $p(t)$ is an unsteady pressure signal and $W^*(t)$ is the complex conjugate of a user-chosen windowing function, which has compact support over a time than the whole $p(t)$ history. The convolution of the shorter window function with the signal produces Fourier transforms of subsets of the full time series. The result is a two-dimensional mapping in the frequency-time domain that provides a measure of the time

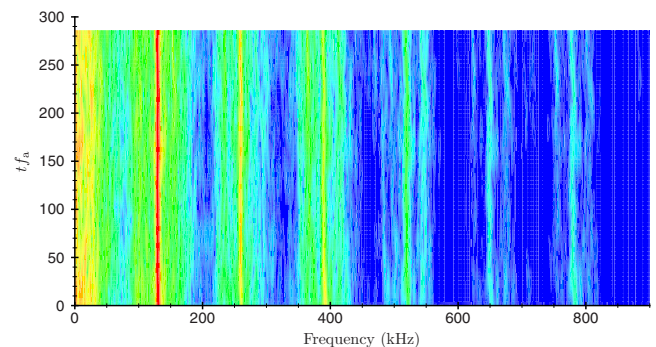


FIG. 4. (Color online) Pressure spectrogram at $(x,y)=(15,-5)\delta_m^0$ for the $L_c/D_c=2$ cavity of the baseline simulation. The vertical axis is plotted with respect to the number of periods of f_a . The shades vary continuously between 40 and 130 dB.

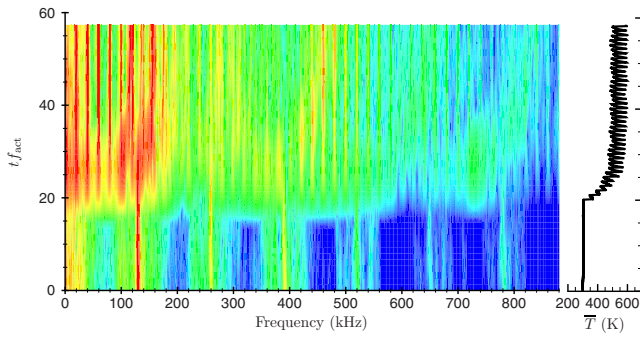


FIG. 5. (Color online) Pressure spectrogram at $(x,y)=(15,-5)\delta_m^0$ for the $L_c/D_c=2$ cavity of the baseline simulation, transitioning to 20 kHz, 10% duty cycle forcing. The vertical axis is plotted with respect to the number of periods of f_{act} . The shades vary continuously between 40 and 130 dB. The temperature of the fluid averaged over the cavity is also plotted for reference on the right of the figure.

evolution of the power spectrum. The square of the magnitude is plotted and is referred to as the pressure spectrogram. The STFT computed for the baseline $L_c/D_c=2$ cavity was obtained with a Fourier transform and a window function size of 18 293 points and the signal was split into segments with 95% overlap. This resulted in the STFT frequency resolution being $\Delta f=1.5$ kHz. A Hanning window was used for $W(t)$. This is plotted for the baseline cavity simulation in Fig. 4. The spectrogram shows that the resonance is stationary, essentially unchanged throughout the time simulated.

Figure 5 shows the joint time-frequency analysis of a simulation started with an already developed baseline flow transitioning to the actuated flow. The actuator model was turned on one-third of the way through the time series and remained on until the end of the simulation. The most obvious feature once the actuation is activated is the appearance of many discrete tones, which are directly associated with the transform of $w(t)$, the time profile of the approximately square-wave plasma model. These appear immediately after the actuator is turned on. More slowly, as the cavity heats up (Fig. 5), the dominant frequencies of the resonance move slightly higher. The principal frequency shifts from 131 to

156 kHz.²⁷ The shift is most visible for the levels shown for the third baseline harmonic. By $tf_a=50$, the gradual drift of the harmonics appears complete.

Though the spectrum is obviously changed significantly by the actuation, the dynamics of the cavity mixing layer structures between actuator firings are barely changed. Figure 6 shows the path of structures traveling along the top of the cavity via the fluctuating pressures for both the baseline and 10% duty cycle cases. The convection velocity of the actuated case is approximately 13% higher than the baseline for the 10% duty cycle forcing, but the structures obviously have a similar character and move in a similar fashion in these two cases. The only substantial effect of the actuation is seen as the actuator fires, which disrupts the nearly periodic feedback and elevates the pressure above the cavity. A tone near the unforced-cavity tone is still apparent in Fig. 5 among the increased energy of other frequencies due to the actuator. We therefore anticipate the effect of the actuator on the downstream flow to predominantly depend on this direct effect of the actuation and we consider this next.

VII. ACTUATOR FORCING MECHANISMS

In this section, we present the investigation of the actuator forcing mechanisms that drive the downstream response observed in experiments.

A. Cavity region visualization: A jetting effect

Several visualizations of the cavity region are presented to show how the actuator forcing creates a perturbation that causes the downstream mixing layer to respond accordingly. We will focus on the actuation with $f_{act}=20$ kHz and a duty cycle of 10%, but will also present some results of simulations with varying duty cycle. We begin by stepping through several discrete times while the actuator is on [the time instants are marked with dots in Fig. 3(a)] and viewing the response of the fluid in the cavity region to the forcing.

Visualizations of the instantaneous velocity vector fields in Figs. 7(a)–7(h) show the two recirculation regions in the cavity, as might be expected for any cavity of aspect ratio

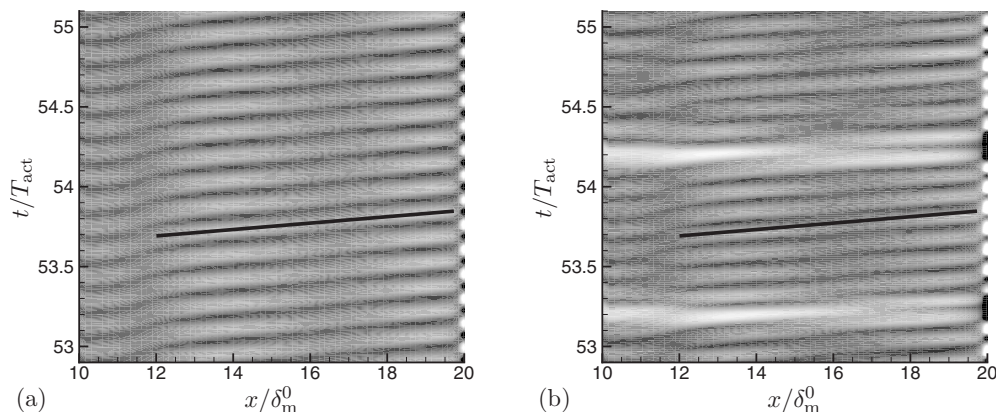


FIG. 6. Pressure evolution at $y=0$ for (a) the baseline and (b) the actuated $L_c/D_c=2$ cavity for two periods of actuator forcing T_{act} near the end of the entire simulation time series for 10% duty cycle forcing. Grayscale levels of the fluctuating pressure over the interval $-0.03 < (p-p_\infty)/\rho_\infty c_\infty^2 < 0.03$ are shown with darker-shaded regions corresponding to $(p-p_\infty)/\rho_\infty c_\infty^2 < 0$. The lines in each pressure field trace the path of a vortical structure traveling over the cavity.

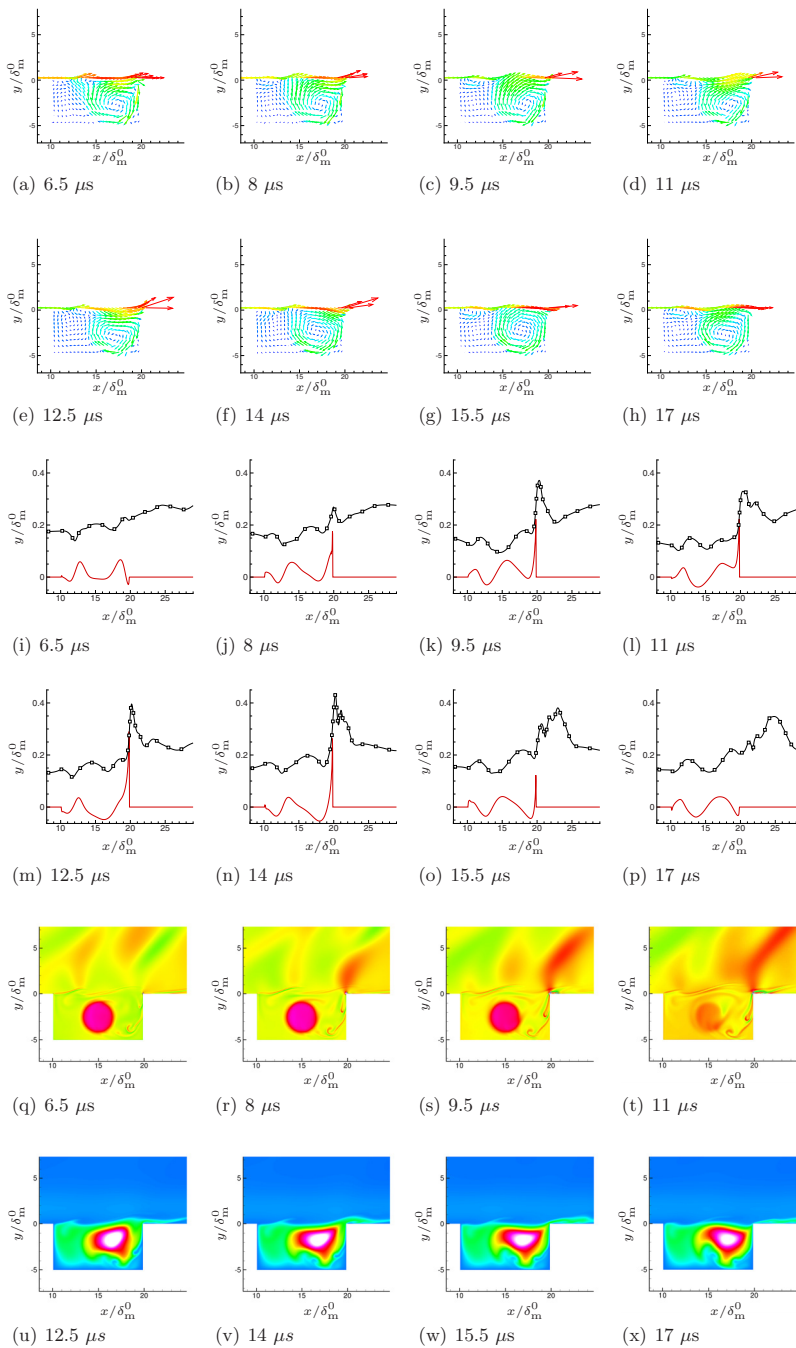


FIG. 7. (Color online) Time series of instantaneous velocity, dilatation, and temperature in the $L_c/D_c=2$ simulation with 10% duty cycle forcing. [(a)–(h)] Velocity vector field of the cavity during actuation. Each vector’s length is proportional to its magnitude. [(i)–(p)] Cross-stream velocity v/c_∞ at $y=0$ from $x=10\delta_m^0$ to $x=30\delta_m^0$, i.e., the top of the cavity along its width to the end of the “nozzle” (—) and the streamwise velocity at $y=0.2\delta_m^0$ (---). [(q)–(t)] Dilatation of velocity with shades varying between $-0.05\delta_m^0/c_\infty < \nabla \cdot \mathbf{u} < 0.05\delta_m^0/c_\infty$. The circular region of positive dilatation corresponds to the actuator model forcing. [(u)–(x)] Temperature fields in the cavity region with shades varying between 235 and 1080 K (white). The times denoted in each figure represent the time after the beginning of the actuator period.

$L_c/D_c=2$. The recirculation is driven, in a sense, by the shear layer above the cavity, which forms at the leading edge where the upstream boundary layer detaches. As the actuator turns on starting at $t=6.5 \mu\text{s}$, the upward fluid motion in the middle of the cavity, which is the upward part of the stronger, clockwise-recirculating flow, appears to be accentuated. A trace of the vertical velocity at $y=0$ at this same time instant is shown in Fig. 7(i). The v -velocity shows two positive regions at $x=13\delta_m^0$ and $x=18\delta_m^0$. These locations correspond to the two vortices forming over the cavity in the growing shear layer and their spacing corresponds to the cavity oscillation frequency of 156 kHz. The velocity vector field begins to show the characteristics of the fluid expanding radially outward from the cavity center. This is seen most clearly by the vectors pointing to the left and up in the top

left quadrant of the cavity ($x < 15\delta_m^0$ and $y > -2.5\delta_m^0$). The cavity is known to be circulating in the counterclockwise direction in this area²⁷ and the velocity induced by the actuator accentuates this recirculation zone.

At $t=8 \mu\text{s}$, as shown in Figs. 7(b) and 7(j), the velocity vectors show the upward action of the recirculating flow and the forcing providing a net movement directly up and out of the cavity. The two vortices have convected further downstream with the first now over the center of the cavity and the second reaching the trailing edge. A spike in both u/c_∞ and v/c_∞ is seen at the trailing edge, suggesting that the shear layer vorticity there is also being displaced up and outward (downstream) by the expanding flow. The velocity vectors confirm this. The circular region of high expansion (shown by positive dilatation of velocity) located in the center of the

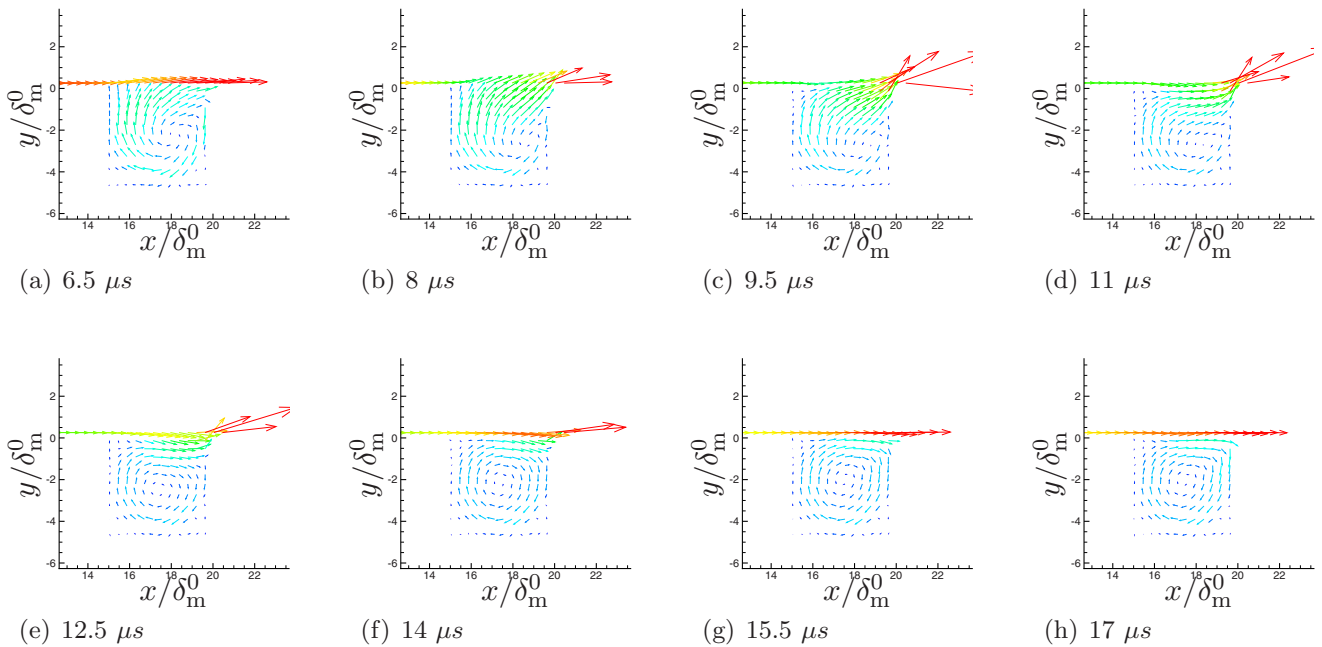


FIG. 8. (Color online) A time series of the velocity vector field of the narrower cavity ($L_c/D_c=1$) during actuation. Each vector's length is proportional to its magnitude. For reference, the dots in Fig. 3(a) mark the times in the forcing period that correspond to the vector fields shown.

cavity, which corresponds to the actuator forcing in Figs. 7(q)–7(t), drives the ejection of fluid out of the cavity.

By $t=9.5 \mu\text{s}$, as seen in Figs. 7(c) and 7(k), the cavity fluid is being ejected from the downstream edge of the cavity in what appears to be a jetting motion. At $t=12.5 \mu\text{s}$, as seen in Figs. 7(e) and 7(m), this ejected fluid has a cross-stream velocity component that is a significant fraction of its stream-wise component. Since the shear layer over the top of the cavity is a significant fraction of the cavity size, the ejected fluid is only pushed into the middle of the downstream boundary layer profile; it remains between the wall and $y=1\delta_m^0$. At this time, the ejected fluid moves at higher velocities (both u and v) than the surrounding fluid. The stream-wise velocity visualized in Figs. 7(k)–7(m) shows that the fluid is not only sent upward by the expansion driving it from below, but it is also displaced forward by the boundary layer velocity pushing it from behind. Because of the thermal input from the actuator over several cycles, the fluid ejected from the cavity is hot and therefore can be clearly seen in the temperature fields in Figs. 7(u)–7(x). Even with obvious stretching and deformation of this ejected fluid by the boundary layer, by $t=14 \mu\text{s}$ there appears in Fig. 7(v) a nearly δ_m^0 thick layer of hot fluid on the wall just downstream of the cavity.

The conclusion of Sec. VI that the natural oscillations are relatively unaffected between actuator firings is consistent with what is seen in Figs. 7(g) and 7(h), which show that another Kelvin–Helmholtz roll-up is already beginning to form over the top of the cavity just after the actuator has shut off.

B. Narrower cavity enhances jetting

The ejection of the fluid from the cavity suggests that part of the actuator's forcing mechanism may resemble more

of a fluidic rather than a thermal actuator. The forcing cycle of the actuator is similar to a synthetic jet in the sense that no net mass is injected, but unlike typical synthetic jet actuators it is driven by the thermal expansion of the local fluid rather than a prescribed mechanical wall motion. Devices similar to LAFPA that cause rapid Joule heating by an electric arc discharge located at the bottom of a finite volume chamber with an orifice at the top also cause an ejection of hot fluid at high velocity.⁸ We can therefore anticipate that if the actuator were more confined, as in a narrower cavity, a stronger ejection might be formed by the thermally induced expansion. This was tested by decreasing L_c from $10\delta_m^0$ down to $5\delta_m^0$, thus making it one-half the width of the OSU cavity with a length-to-depth ratio of $L_c/D_c=1$. In this configuration, the plasma model nearly fills the cavity recess.

Velocity visualizations of this narrow-cavity actuator are shown in Fig. 8. The recirculation in this case is now centered in the cavity. When the actuator is inactive, as seen in Fig. 8(h), there are no obvious instabilities in the velocity field of the detached shear layer of the kind that were evident for the wider cavity as presented in Fig. 7(h), presumably because there is less distance for their amplification. However, when the actuator turns on, Fig. 8(c) shows that there is an even more prominent expulsion of fluid from the downstream edge of the cavity. If this jetting is important for the downstream evolution of the shear layer, we expect there to be a stronger response for this narrower cavity. We investigate this quantitatively in Sec. VII D.

The amount of fluid mass expelled from the cavity when the actuator activates is shown in Fig. 9(a) for both the $L_c/D_c=2$ and $L_c/D_c=1$ cavities. Nearly the same amount of mass is expelled in both cases, peaking just after the end of the period of activation of the actuator, despite the $L_c/D_c=1$ cavity being one-half of the width. The visualizations

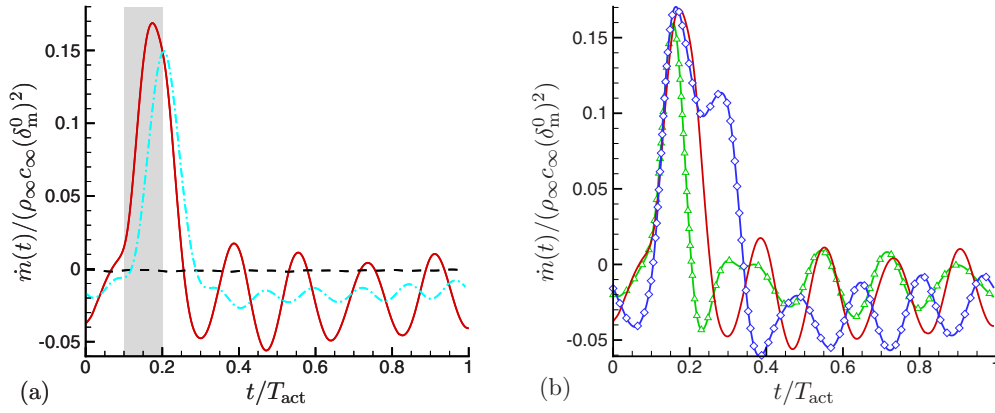


FIG. 9. (Color online) (a) Mass flux (per unit depth) out of the cavity calculated at $y=0$ for the baseline (---), $L_c/D_c=2$ (—), and $L_c/D_c=1$ (-·-) cavities phase-averaged over the forcing frequency f_{act} . The gray region indicates the time the actuator was turned on for 10% duty cycle forcing. (b) Mass flux (per unit depth) as in (a) but for three different duty cycles for the $L_c/D_c=2$ cavity: 5% (—△—), 10% (—), and 20% (—◇—).

show that this ejection is also more focused by the narrower geometry of the cavity. The subsequent oscillations after the ejection as seen in Fig. 9 are the natural instabilities of the cavity and coincide with the dominant fundamental aeroacoustic loop.³⁹ These cavity frequencies are not significant in the pressure spectra of the downstream flow region.²⁷ The wider cavity has significantly stronger fluctuations, presumably because the instabilities of the shear layer can amplify to higher levels before reaching the downstream edge.

Changing the duty cycle of the actuation only weakly affects the peak mass ejection. Ejected mass fluxes for the wider ($L_c/D_c=2$) cavity are shown in Fig. 9(b) for 5%, 10%, and 20% duty cycles. There is more effective mass ejected from the cavity for the larger duty cycles while the actuator is on, but switching from 5% to 10% changes the overall mass ejection relatively little. At 20% duty cycle, it seems that the ejection interacts with the instabilities excited by the dominant cavity oscillation mode, giving the principal ejection another “bump” and putting the subsequent cavity oscillation 180° out of phase with those for lower duty cycle cases. The 20% duty cycle is long enough for two of the vortical roll-ups advecting over the top of the cavity to be pushed upward by the actuation. We will see the ejection of these roll-ups for the 10% duty cycle case in Sec. VII C.

C. Vorticity generation in the near-nozzle region

While it is clear from the OSU experiments that the actuators are indeed effective at exciting the initial shear layers of an axisymmetric jet,⁹ the precise mechanisms of this excitation have been difficult to anticipate. As discussed in Sec. I, the principal effect of the actuator is thought to be thermal heating, so the question of how the actuator works is really how the thermal source comes to alter the vortical development of the downstream shear layer. A baroclinic torque is an obvious candidate, wherein nonparallel pressure and density gradients, for example, can lead to the generation of vorticity and presumably thereby the vortical structures that are seen in a mixing layer. However, boundary layers and free shear layers do not sustain pressure gradients and the visualiza-

tions of the cavity region suggest that the jetting of fluid from the cavity might be the primary mechanism. We see a clear lifting of the boundary layer in Fig. 7, for example. The plasma heating in the cavity space caused a portion of cavity fluid to be ejected from the downstream side of the cavity as we see in the temperature fields of Fig. 7. In this section, we focus on the effect of the actuation on the downstream flow. We again focus on the $L_c/D_c=2$ cavity geometry with 10% duty cycle forcing at 20 kHz.

To investigate the conversion of the imparted thermal energy into vortical disturbances, we appeal to the vorticity evolution equation for a two-dimensional, viscous, compressible fluid. The only nonzero component in two space dimensions is ω_z , which we simply call ω . The governing equation for ω is

$$\frac{\partial \omega}{\partial t} = - \underbrace{(\mathbf{v} \cdot \nabla) \omega}_{\dot{\omega}_A} - \underbrace{\omega (\nabla \cdot \mathbf{v})}_{\dot{\omega}_C} + \underbrace{\frac{1}{\rho^2} \nabla \rho \times \nabla p}_{\dot{\omega}_B} + \underbrace{\nabla \times \left(\frac{\nabla \cdot \boldsymbol{\tau}}{\rho} \right)}_{\dot{\omega}_D}. \quad (5)$$

The terms on the right-hand side are as follows. The first term ($\dot{\omega}_A$) corresponds to vorticity advection via the local flow velocity. The vorticity-dilatation term ($\dot{\omega}_C$) is the product of velocity dilatation ($\nabla \cdot \mathbf{v}$) with vorticity and describes vorticity intensification due to the compressibility of the fluid. The $\dot{\omega}_B$ term is the baroclinic torque and contributes to vorticity generation when density and pressure gradients do not align. The last term is the vorticity diffusion term ($\dot{\omega}_D$) and accounts for diffusion due to viscous effects with $\boldsymbol{\tau}$ the viscous stress.

1. Fluid injection into the boundary layer

We begin by visualizing the terms of the vorticity evolution equation, as well as the flow density, temperature, pressure, and dilatation in Fig. 10. The time chosen here, $t=15.5 \mu\text{s}$, matches the beginning of the actuation cycle and corresponds to the visualizations in Fig. 7(g). The effect of the actuation is the production of significant gradients of

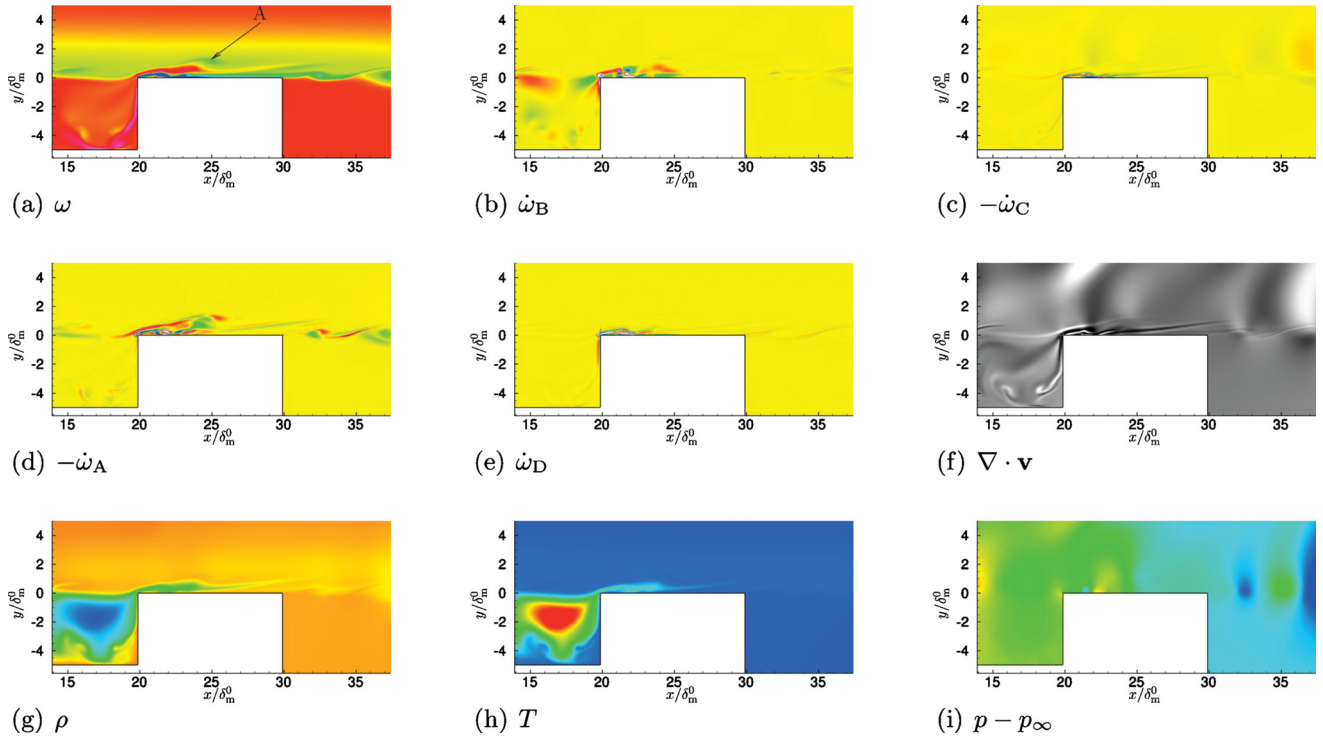


FIG. 10. (Color online) $L_c/D_c=2$ cavity and near-nozzle region $15.5 \mu\text{s}$ after the start of the actuation. (a) ω with shades varying between -1.3 and 0.7 (white). Negative vorticity corresponds to rotation in a clockwise direction. (b) $\dot{\omega}_B$ with shades varying between -0.05 and 0.05 . (c) Negative of $\dot{\omega}_C$ term with shades varying between -0.5 and 0.5 . (d) Negative of $\dot{\omega}_A$ term with shades varying between -0.3 and 0.3 . (e) Dilatation with shades varying between -0.01 (black) and 0.01 (white). (f) Density with shades varying between 0.2 and 1.1 . (g) Temperature with shades varying between 250 and 1000 K. (h) Pressure perturbation with shades varying between -0.1 and 0.1 .

vorticity, density, and temperature in the boundary layer above the wall. The induced thermal expansion of the fluid in the cavity along with the upward flow of the recirculation region cause hot, low density fluid to be ejected from the corner of the cavity into the boundary layer over the wall downstream of the cavity. This process was described by the velocity vector visualizations and mass-flux curves presented in Sec. VII. As visible in the plot of ω in Fig. 10(a), the ejected fluid is relatively irrotational and is forced into the boundary layer in seemingly the same fashion as seen in simulations of synthetic jets actuating flat-plate boundary layers.⁴⁰ Peak streamwise velocity at this time in Fig. 7(o) reaches nearly double the free-stream streamwise velocity at this time and location above the wall. The actuation pushes the hot cavity fluid up into the boundary layer and also forward at a locally higher velocity. The boundary layer is now stratified with colder, denser, high vorticity fluid above and below the ejected fluid. An irrotational layer exists between the shearing mean flow above and the high-shear region below due to the no-slip wall.

The baroclinic torque ($\dot{\omega}_B$) in Fig. 10(b) shows the results of the cross-stream density gradient and a streamwise pressure gradient in the region $20 < x/\delta_m^0 < 25$. However, it is worth mentioning that $\dot{\omega}_B$ is mostly absent beyond this region. We see vortices beginning to form beyond the nozzle edge ($x/\delta_m^0 > 30$) at a spacing determined by the vortex shedding frequency of the cavity. The high rates of change in vorticity at times before the ejected cavity fluid reaches the nozzle edge is mainly the result of the advection term $\dot{\omega}_A$.

Note that the vorticity presented here is negative for clockwise rotation. Therefore, negative dilatation [black regions in Fig. 10(f)] produces negative vorticity in the vorticity-compressibility term in Fig. 10(c) and negative regions of the vorticity-advection term in Fig. 10(d) produce negative vorticity.

We also observe from Fig. 10(a) that the timing of the ejection of fluid by the actuator coincides with the fluid that is periodically ejected by the natural cavity resonance mechanism. The phase-averaged mass-flux profiles presented in Fig. 9 also indicate that the fluid mass ejected by the natural forcing of the cavity oscillations and by the actuator's external forcing tend to coincide. The fluid ejected by the cavity naturally is seen as a higher (more negative) vorticity spot at $(x, y) = (24, 1.5)\delta_m^0$, just above and to the right of the actuator-ejected fluid and labeled as vortex "A" in the figure. Of the sources of vorticity in Eq. (5), only the $\dot{\omega}_A$ term is active at this spot, suggesting that the vorticity is being redistributed by the local flow velocity. There is no baroclinic torque associated with vortex A, since it is not fluid ejected from the cavity interior due to the actuator and thus is of temperature close to the ambient fluid above the cavity.

This reveals that the actuation is, in a sense, lifting the boundary layer up and inserting much hotter fluid (about 40% hotter) than what is carried out of the cavity by the shear layer instabilities forming above it while the actuator is off.

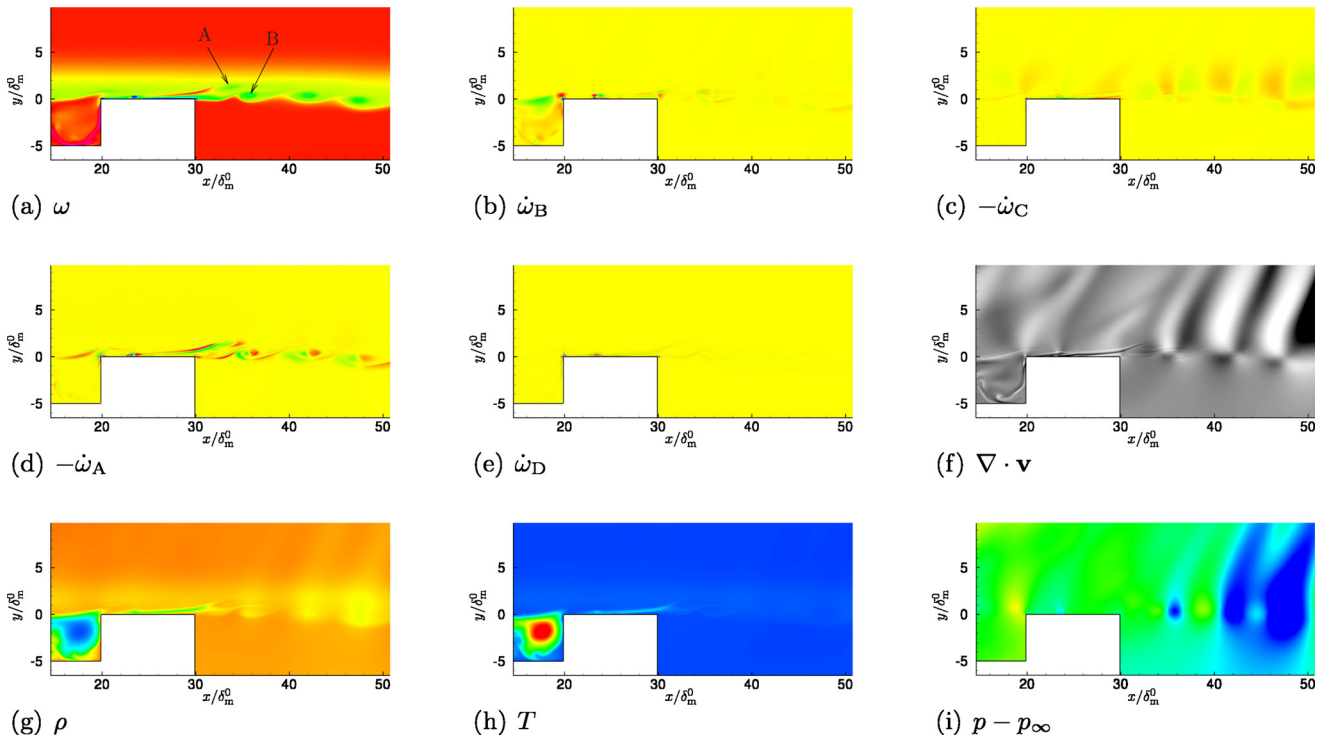


FIG. 11. (Color online) $L_c/D_c=2$ cavity and near-nozzle region $20 \mu\text{s}$ after the start of the actuation. See Fig. 10 for legend and contour values of the fields shown.

2. Boundary layer and nozzle edge interaction

The flow at $t=20 \mu\text{s}$ after the beginning of the firing of the actuator shows the downstream evolution of the nearly irrotational ejected fluid (Fig. 11). It is stretched and elongated rapidly by action of the boundary layer's shear. The shearing has the effect of decreasing the overall wall-normal extent of the ejected fluid, but the low density, high-temperature streak now extends further in the streamwise direction. The maximum temperature of the fluid above the wall downstream of the cavity has decreased to about $T=400 \text{ K}$, with a peak of $T=497 \text{ K}$ at $t=15 \mu\text{s}$. The dilatation is strongly negative in the center of the ejected fluid because of this cooling.

At this time, the baroclinic torque is beginning to make more substantial contributions to the vorticity transport at the nozzle edge. The small positive and negative torque region is visible in Fig. 11(b), just above the edge due to the cross-stream density gradient in the ejected fluid as it reaches this point downstream. The torque is created when the ejected fluid interacts with the pressure difference located at the nozzle edge due to the vortices forming there. As with the visualization in Fig. 10, the time rate of change of the vorticity is still dominated by the vorticity-advection term. The growth of the instability waves in the mixing layer along with the gradual increase in entrained fluid causes the layer to thicken and spread. The $\dot{\omega}_C$ term plotted in Fig. 11(c) does not become significant until locations downstream of the ejected fluid.

Perhaps the largest effect seen here in the visualization is ω in Fig. 11(a). Near $x=33\delta_m^0$, we see the ejected cavity fluid behind the spot of higher vorticity fluid [vortex A in Fig.

10(a)] that was initially an instability wave forming over the cavity by the cavity oscillation feedback loop. The ejection puts this into higher streamwise velocity fluid and pushes it out in front of the ejected hot cavity fluid. We observe this spot being sheared by the boundary layer and moving over the top of one of the vortices forming in the mixing layer. The actuation appears to be causing a forced merging of vortical structures with one that was forming over the cavity (labeled A in the figure). Vortex A was forced forward to interact with a separate vortex forming in the initial downstream mixing layer (labeled "B" in the figure). Figure 12 shows the progression of vortex A as it travels to come into the influence of vortex B for time snapshots between Fig. 10(a) and Fig. 11(a).

3. Vortex roll-up and merging

At $t=26 \mu\text{s}$ after the beginning of the actuation cycle, the effects of the actuation are clearly causing the mixing layer beyond the nozzle to roll-up in a manner different than it does naturally. Visualizations in Fig. 13 show that the hot ejected cavity fluid has been rolled up on itself and has formed a single vortex centered at $x=34\delta_m^0$. The density and temperature fields show that this vortex is relatively low density and high temperature because it contains fluid expelled from the cavity. The baroclinic torque has its highest magnitudes at this time. This suggests that the subsequent roll-up, not the formation, of this vortex is due to the temperature imparted to the boundary layer by the ejected fluid from the actuation. While the baroclinic torque appears to play an important role at this instant, we see in Fig. 11(a) that this vortex was already beginning to separate from vortex B

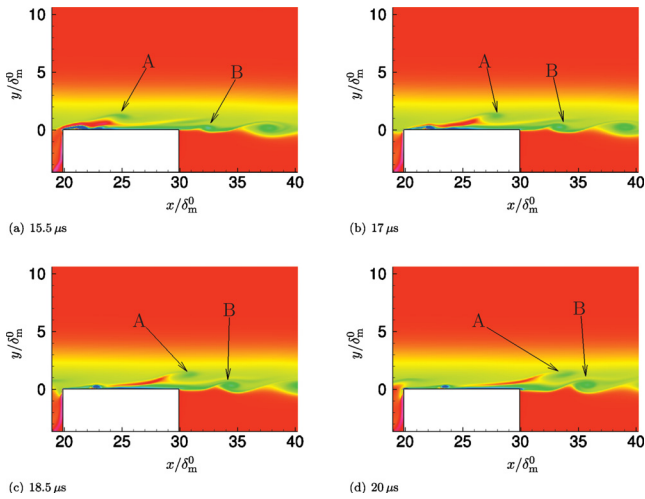


FIG. 12. (Color online) Visualization of the $L_c/D_c=2$ cavity and near-nozzle region for several times after the start of the actuation cycle. ω is shown with shades varying between -1.3 and 0.7 (white). Negative vorticity corresponds to rotation in a clockwise direction. See text for description of labeled vortices A and B.

when the baroclinic torque was not a significant factor in the vorticity transport equation as seen in Fig. 11(b).

The formation of this single vortex appears to be due mainly to the actuation causing the pairing of vortices A and B because of the jetting effect. Vortices A and B denoted in Fig. 11(a) are shown to have reversed order in Fig. 13(a) with vortex B now trailing A. The high velocity fluid created by the actuation that pushed vortex A into the boundary layer has caused it to pass over the top of vortex B. Both of these vortices are now merging with the vortex previously down-

stream of them and beginning to coalesce into one structure. In addition, we also note that between $35 < x/\delta_m^0 < 40$, a braid region appears where the vortex closest to the nozzle edge with high baroclinic torque magnitude is separating from the group of three vortices downstream which include vortices A and B.

In summary, the effect of the actuator in the near field of the nozzle exit appears to be realized by the combination of two factors. First, there is a “forced” pairing caused by the thermally induced expansion in the confined cavity which lifts one of the high vorticity spots (vortex A) associated with the cavity shear layer instability. This region of high vorticity is displaced into the higher-velocity fluid of the boundary layer and interacts with two vortices rolling up in the mixing layer beyond the nozzle exit, causing all three structures to merge together. Second, vorticity is generated by a baroclinic torque just after the nozzle edge, which intensifies rotation of the fluid that has rolled up and separated from the three merging structures just downstream.

We can contrast this with the vortex pairing of the baseline case. Figure 14 shows the space-time evolution of the pressure at $y=0$ (with the mean pressure removed) near the nozzle exit. The intersection of black regions in the figure corresponds to the pairing/merging of vortical structures. The pressure is plotted for the actuation period visualized in the figures of this section of the paper ($0-50 \mu s$) and the next actuation cycle ($50-100 \mu s$).

The baseline simulation shows a regular pattern of pressure perturbations just after the nozzle with a vortex shedding frequency equal to the cavity oscillation frequency. Pairing of the developing vortical structures is seen only rarely and sporadically for $x < 100\delta_m^0$, but the majority of

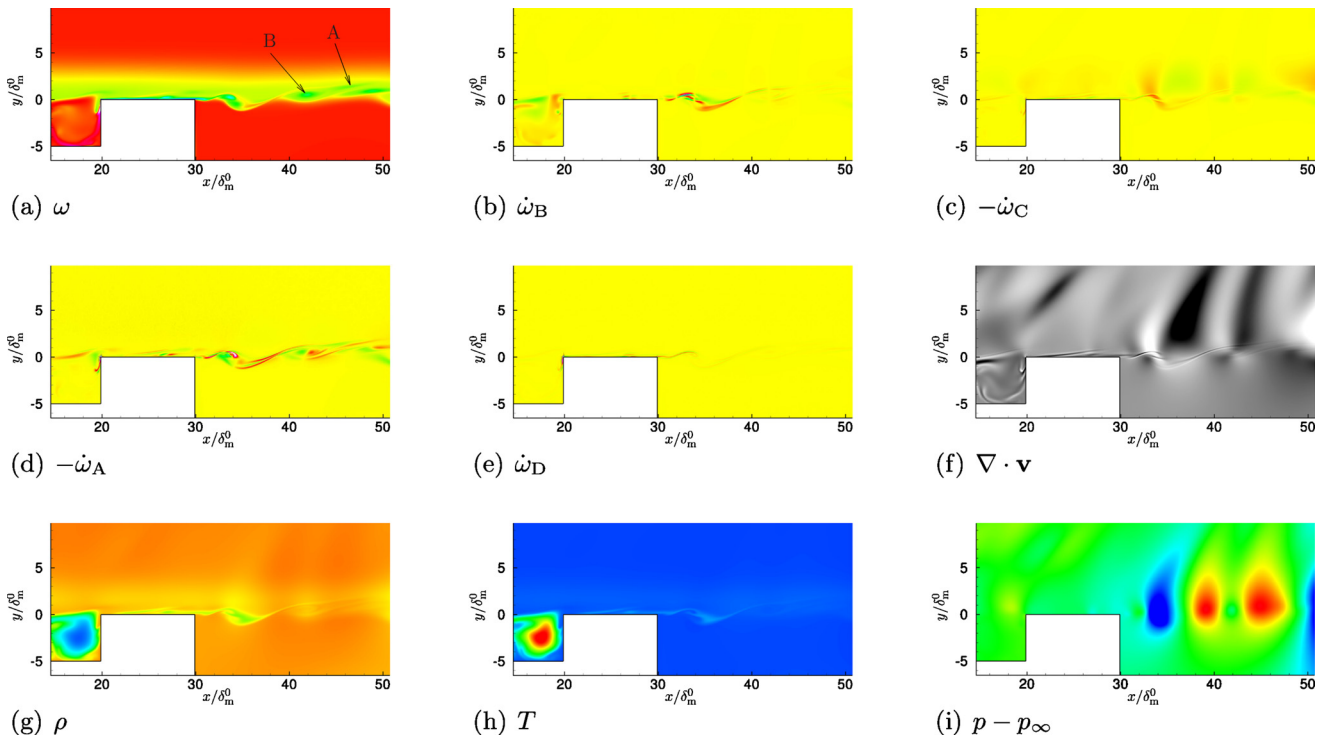


FIG. 13. (Color online) $L_c/D_c=2$ cavity and near-nozzle region $26 \mu s$ after the start of the actuation cycle. See Fig. 10 for legend and contour values of the fields shown.

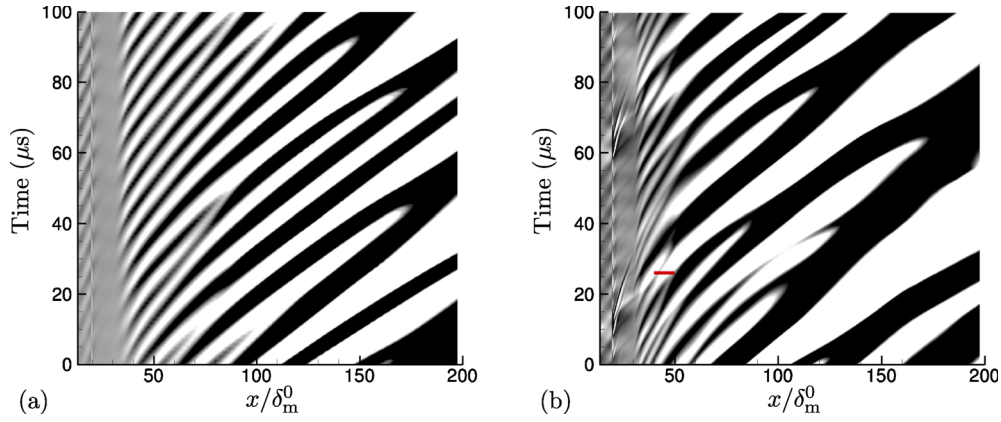


FIG. 14. (Color online) Pressure evolution at $y=0$ for the (a) baseline and (b) actuated $L_c/D_c=2$ cavity for two periods of actuator forcing. Contour levels of the fluctuating pressure over the interval $-0.03 < (p-p_z)/\rho_z c_z^2 < 0.03$ are shown with darker-shaded regions corresponding to $(p-p_z)/\rho_z c_z^2 < 0$ and lighter regions vice versa. The solid horizontal line in (b) corresponds to the location and time of vortices A and B (see text) merging in Fig. 13(a).

pairings occur much farther downstream. On the other hand, the actuated simulation shows a considerable number of pairings even before $x=50\delta_m^0$ including that of vortices A and B with the vortex immediately downstream of them. These three vortices are marked with the solid line in Fig. 14(b) corresponding to their location in Fig. 13(a). The actuation causes pairing to occur far upstream of where they would have occurred without external forcing as indicated by the previous vorticity visualizations.

D. Temperature and cavity effects

Section VII C illuminated two apparent mechanisms by which the actuator affected the cavity and near-nozzle flow. In this section, we assess the relative importance of the higher fluid temperatures created by the actuator forcing versus their mass-source effect due to thermal expansion. The former is responsible for baroclinic torque effects, while the latter is responsible for the ejection behavior we observe. The ejection we see appears to depend on the geometric confinement afforded by the cavity recess. We proceed by introducing several reduced actuator models that are designed to remove either the temperature or the cavity from the full actuator model.

The first model we have developed we refer to as the alternative actuator source model and use it to study the actuator mechanisms with the cavity but in absence of the high temperatures. Using the conservation equations, we aim to provide a similar cavity forcing as S_{act} in Eq. (1), but instead manipulate sources in the equations to produce a comparable pressure response as S_{act} , but without its concomitant rise in temperature. This, of course, requires manipulation of inhomogeneous terms in the governing equations. The conservation equations for the flow density, momentum, and total energy with respective mass, body, and internal energy sources M , F_i , and E are

$$\begin{aligned} \frac{\partial \rho}{\partial t} + \frac{\partial}{\partial x_j}(\rho u_j) &= M, \\ \frac{\partial \rho u_i}{\partial t} + \frac{\partial}{\partial x_j}(\rho u_i u_j) + \frac{\partial p}{\partial x_i} &= F_i, \end{aligned} \quad (6)$$

$$\frac{\partial e}{\partial t} + \frac{\partial}{\partial x_i}[u_i(e+p)] = E.$$

To reach our stated objective, we combine and manipulate these equations to get corresponding equations for the density, pressure, and temperature. The result of this manipulation is

$$\frac{\partial \rho}{\partial t} + u_j \frac{\partial \rho}{\partial x_j} = -\rho \frac{\partial u_j}{\partial x_j} + M,$$

$$\frac{\partial p}{\partial t} + u_j \frac{\partial p}{\partial x_j} = -\gamma p \frac{\partial u_j}{\partial x_j} + (\gamma-1) \left[E - u_j F_j + \frac{1}{2} u_j u_j M \right], \quad (7)$$

$$\frac{\partial T}{\partial t} + u_j \frac{\partial T}{\partial x_j} = -\frac{(\gamma-1)}{T} \frac{\partial u_j}{\partial x_j} + \frac{\gamma}{\rho} \left[E - u_j F_j - \frac{MT}{\gamma} + \frac{1}{2} u_j u_j M \right].$$

Our objective is to match the pressure that results from S_{act} , but without generating significant temperatures. Our target is thus to have

$$T_s = \frac{\gamma}{\rho} \left[E - u_j F_j - \frac{MT}{\gamma} + \frac{1}{2} u_j u_j M \right] = 0, \quad (8)$$

but with the pressure source

$$P_s = (\gamma-1) \left[E - u_j F_j + \frac{1}{2} u_j u_j M \right], \quad (9)$$

designed to generate the same pressure from the actuated simulation. We thus consider P_s to be known, but will need to model it subsequently. By choice, we take $F_j=0$, preferring to work with just M and E . Using Eq. (8) to remove E gives

$$\frac{\gamma}{\rho} \left[\frac{P_s}{(\gamma-1)} - \frac{MT}{\gamma} \right] = 0. \quad (10)$$

Using Eq. (10) we can solve for M and E in terms of the target pressure P_s . The result is

$$M = \frac{\gamma P_s}{(\gamma-1)T},$$

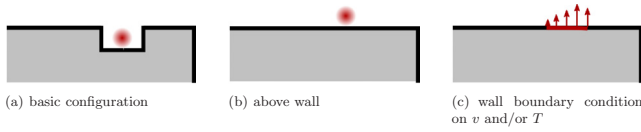


FIG. 15. (Color online) Basic (a) and [(b) and (c)] reduced actuator models.

$$E = \frac{P_s}{(\gamma - 1)} - \frac{1}{2} u_j u_j \frac{\gamma P_s}{(\gamma - 1) T}.$$

We assume that P_s has the same functional form as the actuator forcing source term S_{act} . This way, P_s will have the same dominant pressure spectrum harmonics of f_{act} imparted by the time-dependent portion of the source $w(t)$. S_{act} in the full actuator model is implemented as an internal energy source and therefore it is natural to specify the pressure in terms of internal energy as $S_{\text{act}} = P_s / (\gamma - 1)$. With this, the mass and internal energy sources in the alternative actuator source model are

$$M = \frac{\gamma S_{\text{act}}}{T}, \quad (11)$$

$$E = S_{\text{act}} - \frac{1}{2} u_j u_j \frac{\gamma S_{\text{act}}}{T}. \quad (12)$$

These sources are now added to the governing equations for density and total energy in Eq. (7) and the simulation using this alternate actuator source is carried out as before.

Besides the alternative actuator source model just described, we also have developed three reduced actuator models to estimate the relative importance of the cavity the jetting and the effect of thermal heating on the downstream development of the mixing layer. Instead of specifying a new source model, these models remove the cavity from the simulation completely. In the first, the actuator is placed above the wall, in the experimental configuration for which the plasma appeared to break down as it was advected downstream of the electrodes by the flow.¹⁴ Of course, in the simulation the thermal source does not advect away or break down like an actual plasma. This configuration is shown schematically in Fig. 15(b), where the actuator forcing S_{act} is placed directly in the boundary layer flow, centered at $(x_{\text{act}}, y_{\text{act}}) = (15, 5) \delta_m^0$.

In the two other cases, both shown schematically in Fig. 15(c), the $L_c/D_c = 2$ cavity is replaced with a wall boundary condition with either the wall-normal v velocity or both v and temperature T taken from the full actuator simulation. For this boundary condition actuation, the needed data from the full cavity simulation were saved every 100 time steps and cubic splines were used to interpolate it to provide the time-dependent wall boundary conditions. The Navier–Stokes characteristic boundary conditions were used to solve for the density on the wall in the same manner as it is solved everywhere else on the wall (see Sec. IV B). However, the streamwise velocity u was set to zero as per the no-slip condition. Imposing only v on the wall is loosely thought of as imposing a blowing/suction type boundary condition while omitting the effects of heating and the cavity. The advecting

v -velocity fluctuations associated with the forming instabilities over the cavity are present in the boundary condition data, so this forcing is not a traditional blowing/suction boundary condition. Prescribing v and T was done to remove the cavity effects but still maintain the jetting and heating components of the actuation.

We compare these various actuator models and geometry configurations in Fig. 16(a) by presenting the momentum thickness of the downstream mixing layer for all of the simulations along with the baseline case. As expected, all of the actuated cases spread more than the baseline, but none of the reduced or alternative actuators match the spreading caused by the full actuator with the cavity. The fastest spread is for the narrow-cavity case, for which we anticipated improved response based on the apparently stronger ejection of fluid out of the cavity. The narrow cavity increases the spreading by nearly 50% over the baseline case.

The actuator placed above the wall is seen to be the least effective of all. This behavior suggests that the cavity geometry is indeed necessary for eliciting a mixing layer response, beyond its role in stabilizing the plasma. This configuration does not allow for high temperatures to be retained from one actuation cycle to the next since all of the fluid heated by S_{act} is swept immediately downstream. The maximum fluid temperature generated by the actuation in this forcing configuration is 355 K at $(x_{\text{act}}, y_{\text{act}})$ or about 18% higher than T_∞ . The v -only case yields almost an identically weak response downstream compared to the case with the actuator placed above the wall.

The mixing layer responds more strongly with both v and T wall forcing, suggesting some explicit thermal or density role in the subsequent amplification of the disturbances. The alternative actuator source causes almost the same mixing layer growth response as only specifying v and T up until $x = 150 \delta_m^0$, where the alternative source simulation encounters a decrease in growth rate.

The alternative source and the full actuator source have similar growth responses even though the alternative source was designed to not produce the high temperatures created by S_{act} . Figure 17 shows the fluid temperature evolution over the cavity and nozzle edge for all of the simulations at 20 μs after actuation (the same time as Fig. 11). The temperature is reduced by approximately 30% between the alternative source and the v and T reduced actuator above the nozzle wall. We see that the alternative source model is successful in suppressing high temperatures associated with the full actuator model. From Fig. 17, it is clear that the high fluid temperature (as high as 1800 K) in the cavity is significantly reduced by the time it is ejected from the cavity and begins to interact with the surrounding flow.

The disparity in temperature between the alternative source and simulations with a cavity suggests that the effectiveness of the actuator forcing in causing the downstream growth increase of the mixing layer is not directly due to its thermal forcing. Instead, the strength of the generated baroclinic torque appears to have a relationship with the observed growth response downstream. Figure 18 shows the baroclinic term of the narrow cavity and other model simulations just as the first roll-up generated by the actuation (in the full cavity

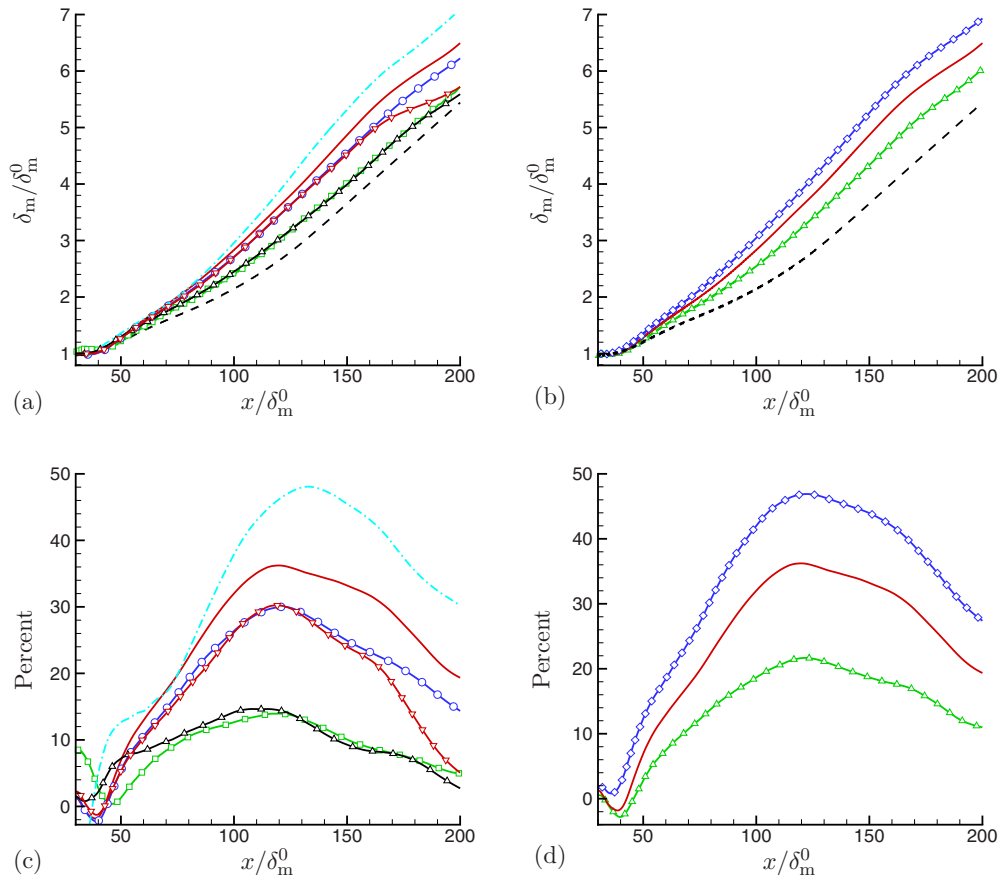


FIG. 16. (Color online) (a) Momentum thickness of the various simulations with and without the cavity with 10% duty cycle forcing. Curves indicate: baseline (---), full cavity simulation (—), no cavity with v imposed (\square -), no cavity with temperature and v imposed (\circ -), narrow-cavity ($L_c/D_c=1$) simulation (-.-), actuator above wall (\triangle -), and alternative actuator source (∇ -). (b) Momentum thickness for simulations with three different duty cycles for the $L_c/D_c=2$ cavity: 5% (\triangle -), 10% (—), 20% (\diamond -), and baseline (no actuation) for comparison (---). Percent increase in momentum thickness over the baseline case for the (c) 10% duty cycle cases and for (d) three duty cycles.

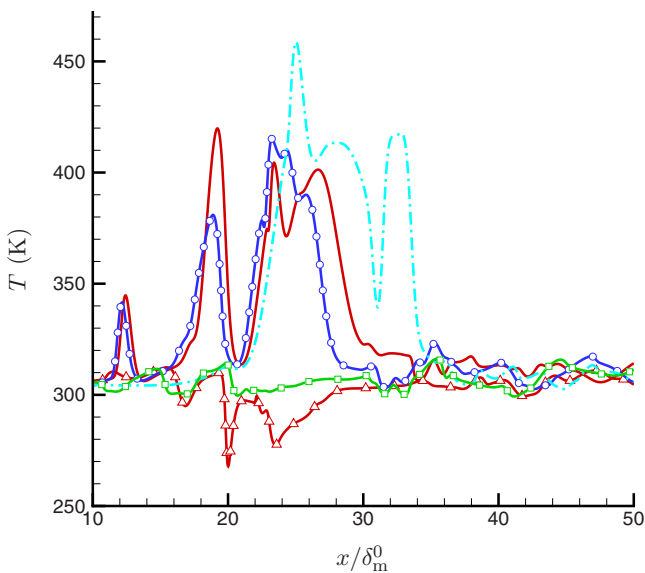


FIG. 17. (Color online) Fluid temperature of the simulations with 10% duty cycle forcing with and without the cavity just above the nozzle wall at $y=0.25\delta_m^0$ and $20\ \mu\text{s}$ after actuation. Curves indicate: full cavity simulation (—), no cavity with v imposed (\square -), no cavity with temperature and v imposed (\circ -), narrow-cavity ($L_c/D_c=1$) simulation (-.-), and alternative actuator source (\triangle -).

simulations) occurs. The snapshots of $\dot{\omega}_B$ are ordered from (a) to (f) from highest torque magnitude ($\sqrt{\dot{\omega}_B^2}$) occurring after $x=30\delta_m^0$ to the lowest, respectively. For most of the cases, the higher $\dot{\omega}_B$ have the strongest downstream spreading in the mixing layer and decreasing torque is correlated with a decreased downstream growth. However, the maximum torque magnitude for the alternative source is about two and a half times smaller than the maximum torque magnitude in the v and T case, suggesting again that the thermal component of the actuator forcing is a secondary mechanism to the jetting fluid exiting the cavity. While greater baroclinic torques appear to correlate to larger growth rates for the simulations with the cavity, the alternative source and the v and T wall forcing grow with almost identical rates.

The essential difference between the v and T wall forcing and the full actuator simulation of the $L_c/D_c=2$ cavity is the removal of the streamwise velocity component above the cavity. Not including this streamwise velocity causes a reduction in growth rate on par with not ejecting fluid from the cavity at high temperature according to Fig. 16(a). In Fig. 19, we see the instantaneous cross-stream and streamwise velocity traces for the 10% duty cycle simulations just above the wall. These traces are shown just as the fluid ejected out of the cavity by the actuator is pushed above the nozzle wall and before the boundary layer flow significantly deforms it.

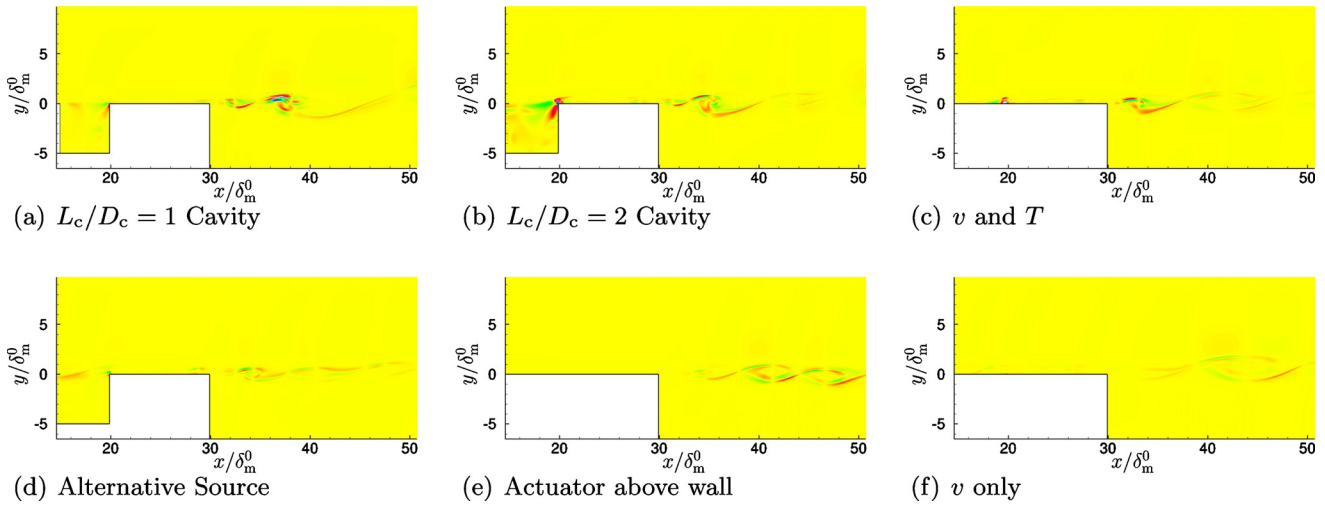


FIG. 18. (Color online) Baroclinic torque (ω_B) in the near-nozzle region $26 \mu s$ after the start of the actuation cycle for the actuated simulations with 10% duty cycle. Shades vary between 0.05 and -0.05 .

We have seen in Sec. VII A from the velocity vector visualizations and mass-flux profiles that the vertical velocity is an indicator of the cavity’s fluid ejection and, now, Fig. 19(b) shows that the actuation provides significant streamwise velocity augmentation as well. The trend of u -velocity magnitude follows the same trend of downstream mixing layer growth. While the v and T wall forcing and the full L_c/D_c

$=2$ cavity simulation have identical v velocities (by design), the streamwise velocity is reduced for the wall forcing to levels below that of the alternative source.

The effect of duty cycle on momentum thickness for the full actuator in the $L_c/D_c=2$ cavity is shown in Fig. 16(b). We see an increase in response with increasing duty cycle and the mechanisms for this follow the same trends revealed

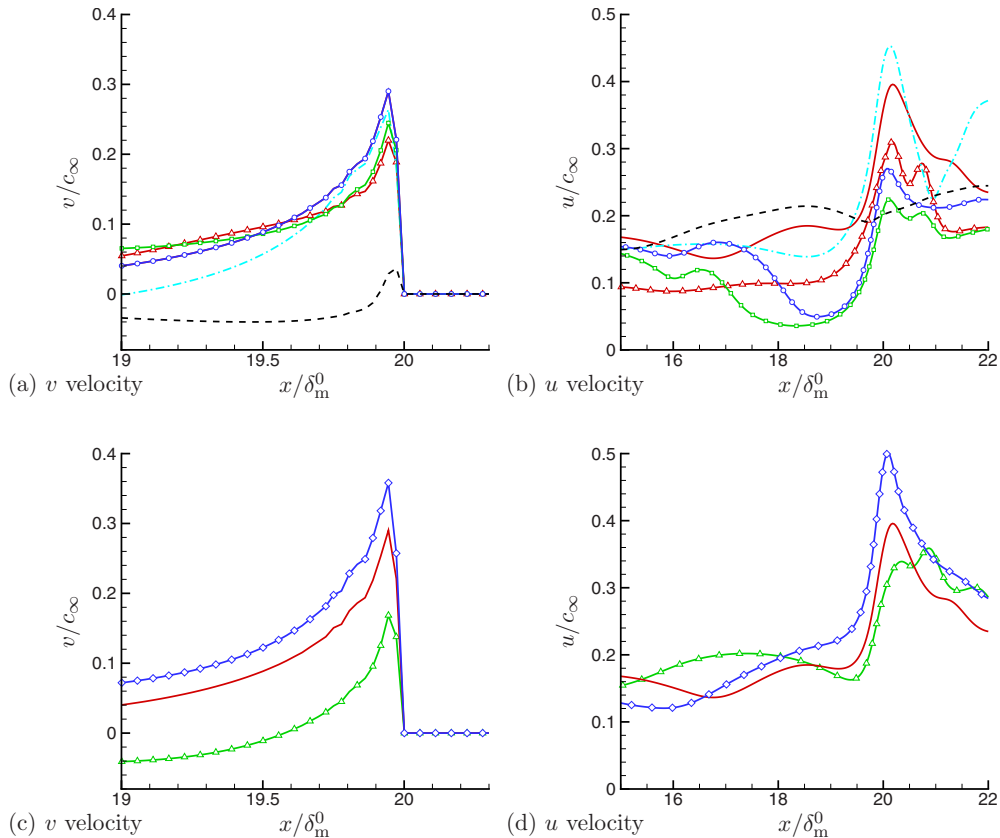


FIG. 19. (Color online) [(a) and (c)] Profiles of v -velocity at $y=0$ and [(b) and (d)] u -velocity at $y=0.25\delta_m^0$ at $t=12.5 \mu s$ after actuation. For the curves in (a) and (b): baseline (---), full cavity simulation (—), no cavity with v imposed (\square -), no cavity with temperature and v imposed (\circ -), narrow-cavity ($L_c/D_c=1$) simulation (\dashv -), and alternative actuator source (∇ -). For the curves in (c) and (d): 5% duty cycle (\triangle -), 10% (—), 20% (\diamond -).

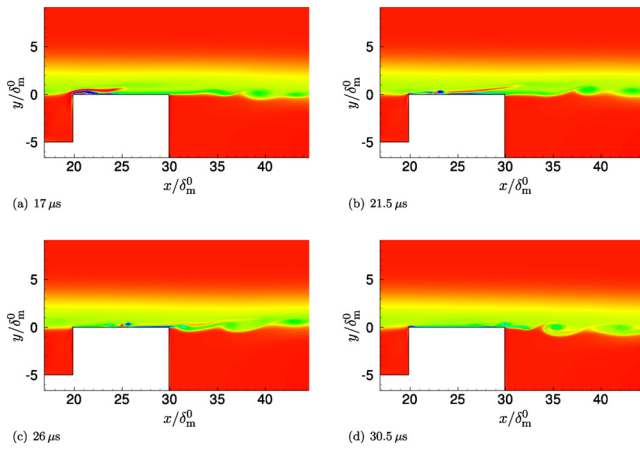


FIG. 20. (Color online) $L_c/D_c=2$ cavity and near-nozzle region at several times after the start of the actuation cycle for the alternative actuator source. ω with shades varying between -1.3 and 0.7 . Negative vorticity corresponds to rotation in a clockwise direction.

with the different actuator models. As the length of actuator on-time increases, the velocities that eject the fluid also increase and cause the mixing layer to grow faster. The 20% duty cycle forcing and the narrower $L_c/D_c=1$ cavity forced at 10% spread at almost the same rates, suggesting that the narrow cavity would provide similar control response for lower input power requirements.

The perturbation to the boundary layer is primarily due to the fluid ejected from the cavity recess. Mixing layers have long been known to be highly susceptible to this type of upstream forcing with modest responses realizable with $u'/U_\infty \approx 10^{-2}$ for a perturbation velocity u' and as low as 10^{-7} if the forcing is near the natural frequency of the layer.⁴¹ From the instantaneous values shown in Fig. 19, the forcing provided by the actuator model is about $u'/U_\infty = 10^{-1}$ for both the v and u velocity increases above the baseline. The hot ejected fluid is deformed by the boundary layer and a region of high vorticity is concentrated just after the nozzle wall resulting in an immediate roll-up and the first sign of mixing layer response to forcing.

The baroclinic term in the vorticity evolution equation is active in the nozzle edge region due to the temperature difference between the ejected fluid and the surroundings. However, the alternative actuator source, which was designed to force at similar but lower temperatures, still causes the immediate roll-up as seen by vorticity visualizations in Fig. 20 despite significantly smaller baroclinic torque magnitude [see Fig. 18(d)]. Reduced actuator models, which forced with only v -velocity and v -velocity and temperature without the cavity, yield a diminished mixing layer response downstream. Figure 19 suggests that the cavity is essential in producing both u and v to achieve maximum mixing layer response. Increasing the actuation duty cycle and reducing the cavity length increase the mixing layer spreading through higher perturbation velocities, suggesting again that the baroclinic torque due to the actuator is not as critical as the jetting effect.

VIII. CONCLUSIONS

Our model actuators were designed to match the geometry and flow parameters, including Reynolds number, of the ongoing OSU actuated jets.⁹ The model was simplified by having the actuation be a simple thermal source and was two-dimensional to ease computational expense, though this was still nontrivial, requiring 3×10^6 mesh points and millions of numerical time steps to achieve a quasistationary actuation and converge statistics. The actual actuators are, of course, three-dimensional, but the model includes the key features of the system: the boundary layer, actuator cavity recess, and the nozzle lip. Joule heating is thought to be the principal action of the plasma. Despite this obvious limitation, the model actuators matched well both the measured temperature in the cavity and the near-field pressure intensity associated with their firing. Any lateral ejection of fluid they might cause in a three-dimensional geometry, which would correspond more closely to the corresponding experiments, will of course be missed. Similarly, there is no possibility of representing any effects associated true three-dimensional turbulence.

The results of the simulations have illuminated several features of the actuation. The forcing supplied by the plasma actuator model causes a locally high-temperature recirculating region of fluid centered in the cavity. When the actuator fires, a sudden fluid expansion occurs in the cavity, which lifts the shear layer that has formed over the cavity and injects hot fluid into the boundary layer. The cavity is essential for producing this effect. The jetting effect provides the perturbation to the flow that causes the main response downstream of the nozzle exit. Higher temperatures created by the plasma also appear to be correlated with the increased response of the downstream flow, but are unnecessary for strong forcing. Forcing with the narrower cavity also produced stronger jetting effects, seemingly because of the increased ejection of fluid in this case.

An alternative actuator source model was designed to provide a similar pressure response in the cavity as the full plasma model source, but without significant heating. A simulation with this alternative actuator model still provided significant excitation of the mixing layer and organized downstream flow structures but at temperatures close to the ambient flow. It appears that the increased temperatures lead to some vortical effect via a baroclinic torque; however, the approximately isothermal alternative source showed significantly reduced magnitudes of this torque with only marginal loss of control authority. This leads us to conclude that the jetting promoted by the cavity is the primary means by which the actuator causes the flow response. Optimization of this cavity to harness this effect should improve the effectiveness of such actuators.

Recently, it has been found with lower frequency of forcing (3.5 Hz) with these same actuators of a Mach 0.9 jet that lower duty cycles lead to greater downstream response.⁴² Unfortunately, the flow and actuation conditions are different and there are no data available for the near-nozzle region we study. However, the ejection mechanism we observe might be consistent with this: the cooler the fluid

in the cavity recess when the actuator fires, the more it can potentially expand when heated by the plasma perhaps leading to the greater authority. However, very near the nozzle our higher frequency actuator model suggests the opposite response. Hopefully, improved diagnostics and further simulations will clarify this.

ACKNOWLEDGMENTS

This work was supported by NASA Glenn Research Center (NNX07AC86A). The authors thank Professor Samimy of OSU for helpful tips and discussion.

- ¹M. Samimy, K. B. M. Q. Zaman, and M. Reeder, "Effect of tabs on the flow and noise field of an axisymmetric jet," *AIAA J.* **31**, 609 (1993).
- ²M. F. Reeder and M. Samimy, "The evolution of a jet with vortex generating tabs: Real-time visualization and quantitative measurements," *J. Fluid Mech.* **311**, 73 (1996).
- ³K. B. M. Q. Zaman, "Spreading characteristics of compressible jets from nozzles of various geometries," *J. Fluid Mech.* **383**, 197 (1999).
- ⁴C. K. W. Tam, "Influence of nozzle geometry on the noise of high-speed jets," *AIAA J.* **36**, 1396 (1998).
- ⁵C. K. W. Tam and K. B. M. Q. Zaman, "Subsonic jet noise from non-axisymmetric and tabbed nozzles," AIAA Paper No. 2000-0086, 2000.
- ⁶B. Callender, E. Gutmark, and S. Martens, "Far-field acoustic investigation into chevron nozzle mechanisms and trends," *AIAA J.* **43**, 87 (2005).
- ⁷A. Glezer and M. Amitay, "Synthetic jets," *Annu. Rev. Fluid Mech.* **34**, 503 (2002).
- ⁸B. Cybyk, K. Grossman, and D. V. Wie, "Computational assessment of the spark jet flow control actuator," AIAA Paper No. 2003-3711, 2003.
- ⁹M. Samimy, J. H. Kim, J. Kastner, I. Adamovich, and Y. Utkin, "Active control of high-speed and high-Reynolds-number jets using plasma actuators," *J. Fluid Mech.* **578**, 305 (2007).
- ¹⁰T. Corke and M. Post, "Overview of plasma actuators: Concepts, optimization, and applications," AIAA Paper No. 2005-0563, 2005.
- ¹¹R. L. Kimmel, J. R. Hayes, J. A. Menart, and J. Shang, "Effect of surface plasma discharges on boundary layers at mach 5," AIAA Paper No. 2004-0509, 2004.
- ¹²S. Merriman, E. Ploenjes, P. Palm, and I. Adamovich, "Shock wave control by nonequilibrium plasmas in cold supersonic gas flows," *AIAA J.* **39**, 1547 (2001).
- ¹³M. Samimy, I. Adamovich, B. Webb, J. Kastner, J. Hileman, S. Keshav, and P. Palm, "Development and characterization of plasma actuators for high speed and Reynolds number jet control," *Exp. Fluids* **37**, 577 (2004).
- ¹⁴Y. G. Utkin, S. Keshav, J. Kim, J. Kastner, I. V. Adamovich, and M. Samimy, "Development and use of localized arc filament plasma actuators for high-speed flow control," *J. Phys. D: Appl. Phys.* **40**, 685 (2007).
- ¹⁵T. C. Corke, M. L. Post, and D. M. Orlov, "SDBD plasma enhanced aerodynamics: Concepts, optimization and applications," *Prog. Aerosp. Sci.* **43**, 193 (2007).
- ¹⁶S. O. Macheret, M. N. Schneider, and R. B. Miles, "Magnetohydrodynamic and electrohydro-dynamic control of hypersonic flows of weakly ionized plasmas," *AIAA J.* **42**, 1378 (2004).
- ¹⁷S. Leonov, V. Biturkin, D. Yarantsev, and A. Youriev, "The effect of plasma induced separation," AIAA Paper No. 2003-3853, 2003.
- ¹⁸M. Samimy, J.-H. Kim, I. Adamovich, Y. Utkin, and J. Kastner, "Towards noise mitigation in high speed and high Reynolds number jets using plasma actuators," AIAA Paper No. 2006-2703, 2006.
- ¹⁹J. H. Kim, I. Adamovich, and M. Samimy, "Active noise control in a Mach 1.3 ideally-expanded jet with plasma actuators," AIAA Paper No. 2008-0038, 2008.
- ²⁰D. V. Gaitonde, "Simulation of supersonic nozzle flows with plasma-based control," AIAA Paper No. 2009-4187, 2009.
- ²¹J. S. Shang, S. T. Surzhikov, R. Kimmel, D. Gaitonde, J. Menart, and J. Hayes, "Mechanisms of plasma actuators for hypersonic flow control," *Prog. Aerosp. Sci.* **41**, 642 (2005).
- ²²M. Samimy, "Preliminary results on characterization of LAFPA's," Gas Dynamics and Turbulence Laboratory, The Ohio State University (internal document).
- ²³C. Lui, "A numerical investigation of shock-associated noise," Ph.D. thesis, Stanford University, 2003.
- ²⁴J. Kastner, J. Hileman, and M. Samimy, "Exploring high-speed axisymmetric jet noise control using Hartmann tube fluidic actuators," AIAA Paper No. 2004-0186, 2004.
- ²⁵K. Viswanathan and L. T. Clark, "Effect of nozzle contour on jet aerodynamics," AIAA Paper No. 2004-0008, 2004.
- ²⁶M. Kearney-Fischer, J.-H. Kim, and M. Samimy, "Control of a high Reynolds number mach 0.9 heated jet using plasma actuators," *Phys. Fluids* **21**, 095101 (2009).
- ²⁷R. R. Kleinman, "On the turbulence-generated sound and control of compressible mixing layers," Ph.D. thesis, University of Illinois, Urbana, IL, 2010.
- ²⁸T. J. Poinsot and S. K. Lele, "Boundary-conditions for direct simulations of compressible viscous flows," *J. Comput. Phys.* **101**, 104 (1992).
- ²⁹C. S. Yoo and H. G. Im, "Characteristic boundary conditions for simulations of compressible reacting flows with multi-dimensional, viscous and reaction effects," *Combust. Theory Modell.* **11**, 259 (2007).
- ³⁰J. B. Freund, "Proposed inflow/outflow boundary condition for direct computation of aerodynamic sound," *AIAA J.* **35**, 740 (1997).
- ³¹D. J. Bodony, "Analysis of sponge zones for computational fluid mechanics," *J. Comput. Phys.* **212**, 681 (2006).
- ³²S. Lele, "Compact finite-difference schemes with spectral-like resolution," *J. Comput. Phys.* **103**, 16 (1992).
- ³³R. R. Kleinman and J. B. Freund, "The sound from mixing layers simulated with different ranges of turbulence scales," *Phys. Fluids* **20**, 101503 (2008).
- ³⁴M. Samimy, J. Kastner, J.-H. Kim, Y. Utkin, I. Adamovich, and C. Brown, "Flow and noise control in high speed and high Reynolds number jets using plasma actuators," AIAA Paper No. 2006-2846, 2006.
- ³⁵J. E. Rossiter, "Wind-tunnel experiments on the flow over rectangular cavities at subsonic and transonic speeds," NASA Ames Research Center R&M No. 3438, October 1964.
- ³⁶M. Gharib and A. Roshko, "The effect of flow oscillations on cavity drag," *J. Fluid Mech.* **177**, 501 (1987).
- ³⁷C. W. Rowley, T. Colonius, and A. J. Basu, "On self-sustained oscillation in two-dimensional compressible flow over rectangular cavities," *J. Fluid Mech.* **455**, 315 (2002).
- ³⁸C. K. W. Tam and P. J. W. Block, "On the tones and pressure oscillations induced by flow over rectangular cavities," *J. Fluid Mech.* **89**, 373 (1978).
- ³⁹N. Delprat, "Rossiter's formula: A simple spectral model for complex amplitude modulation process?," *Phys. Fluids* **18**, 071703 (2006).
- ⁴⁰R. Mittal, P. Rampunggoon, and H. S. Udaykumar, "Interaction of a synthetic jet with a flat-plate boundary layer," AIAA Paper No. 2001-2773, 2001.
- ⁴¹C.-M. Ho and P. Heurre, "Perturbed free shear layers," *Annu. Rev. Fluid Mech.* **16**, 365 (1984).
- ⁴²M. Samimy (personal communication, 2010).